

# Diff-Reg v1: Diffusion Matching Model for Registration Problem

Qianliang Wu, Haobo Jiang, Lei Luo, Jun Li, Yaqing Ding, Jin Xie, Jian Yang

**Abstract**—Establishing reliable correspondences is essential for registration tasks such as 3D and 2D3D registration. Existing methods commonly leverage geometric or semantic point features to generate potential correspondences. However, these features may face challenges such as large deformation, scale inconsistency, and ambiguous matching problems (e.g., symmetry). Additionally, many previous methods, which rely on single-pass prediction, may struggle with local minima in complex scenarios. To mitigate these challenges, we introduce a diffusion matching model for robust correspondence construction. Our approach treats correspondence estimation as a denoising diffusion process within the doubly stochastic matrix space, which gradually denoises (refines) a doubly stochastic matching matrix to the ground-truth one for high-quality correspondence estimation. It involves a forward diffusion process that gradually introduces Gaussian noise into the ground truth matching matrix and a reverse denoising process that iteratively refines the noisy matching matrix. In particular, the feature extraction from the backbone occurs only once during the inference phase. Our lightweight denoising module utilizes the same feature at each reverse sampling step. Evaluation of our method on both 3D and 2D3D registration tasks confirms its effectiveness. The code is available at <https://github.com/wuqianliang/Diff-Reg>.

**Index Terms**—3D Registration, 2D3D Registration, Diffusion model, Doubly Stochastic Matrix Space.

## I. INTRODUCTION

**T**he 3D registration problem, encompassing point cloud registration and image-to-point-cloud registration is critical in various computer vision and computer graphics applications, including 3D reconstructions, localization, and robotics. These applications usually necessitate precise correspondences (matchings) between point cloud pairs or image-to-point-cloud pairs for reliable rigid transformation or non-rigid deformation estimations.

The goal of achieving accurate matchings is to identify the most significant correspondences [1]–[3] with local or global semantic or geometric consistency [4]–[7]. However, this objective would be challenging especially in situations with globally ambiguous matching patches, large deformation, scale inconsistency, and low overlapping problems (refer to Fig.1).

Recently, deep learning-based feature matching methods [2], [4], [6], [8]–[13] have achieved significant progress in point cloud registration by employing UNet-like [14], [15] backbones to extract superpoints (subsamped patches) and

their associated features. These methods typically compute an initial matching matrix between superpoints in the feature space. Additionally, outlier rejection techniques [16]–[20] propose specialized methodologies to identify improved inlier correspondences based on certain semantic or geometric priors [1], [7], [21], [22]. However, these methods usually rely on a single-pass prediction of correspondences, which may not always yield optimal results.

In this paper, drawing inspiration from the diffusion model [23]–[26], we introduce a diffusion matching model in the doubly stochastic matrix space [27] to progressively denoise (refine) the matching matrix to the optimal one for robust correspondence estimation. By training a diffusion model with the doubly stochastic matrix space as a feasible solution domain, we effectively learn a generalized optimization algorithm specifically designed for the doubly stochastic matrix space, adapted to the characteristics of the dataset or scene. Since the doubly stochastic matrix space is a convex set, the diffusion model can find the optimal solution by leveraging the learned “direction”. Our diffusion matching model consists of two main components: a forward diffusion process and a reverse denoising process, which operates within the matrix space. The forward diffusion process gradually introduces Gaussian noise into the ground truth matching matrix, while the reverse denoising process iteratively refines the noisy matrix to the optimal one. For efficiency, we propose a novel and generalized lightweight denoising module that can be adapted to 2D2D image matching, 2D3D, and 3D registration tasks.

Finally, we establish a specific variational lower bound associated with our diffusion matching model in the doubly stochastic matrix space and a simplified version of the objective function to train our framework effectively.

### **Why diffused in the doubly stochastic matrix space?**

Tasks such as image or point cloud registration face challenges like scale inconsistency, large deformation, ambiguous matching, and low overlapping. Several state-of-the-art (SOTA) studies [6], [7], [13], [17], [20], [28], [29] have attempted to encode high-order combinational geometric consistency. However, these manually crafted designs may not encompass all potential effective strategies for various challenging scenarios (e.g., large deformation). The diffusion process in the matrix space serves as a practical data augmentation technique that can generate additional training samples incorporating any-order combinational consistency, offering a promising approach to address these challenges.

Our approach presents several advantages compared to previous registration methods. The forward diffusion process

Qianliang Wu, Haobo Jiang, Lei Luo, Jun Li, Yaqing Ding, Jin Xie, and Jian Yang are with PCA Lab, Key Lab of Intelligent Perception and Systems for High-Dimensional Information of Ministry of Education, and Jiangsu Key Lab of Image and Video Understanding for Social Security, School of Computer Science and Engineering, Nanjing University of Science and Technology.

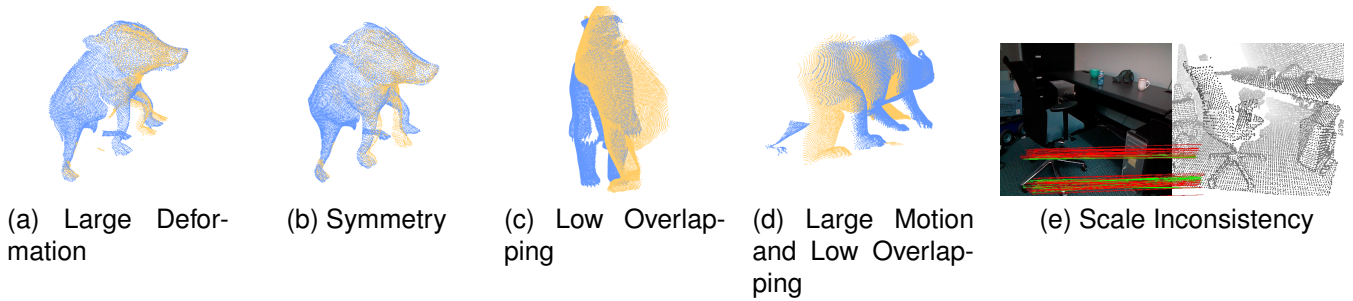


Fig. 1. Some challenges in 3D (and 2D3D) registration problem. (d) Presence of both low overlapping and large deformation issues simultaneously. (e) Losing the correspondence far from the camera. Please zoom in for details.

generates diverse training samples, acting as data augmentation for the feature backbone and single-pass prediction head, thus improving the model’s generalization capability. In contrast, the drawback of one-pass prediction methods is that if correspondences are predicted in a local minimum, subsequent outlier rejection or post-processing steps may face significant challenges. Our reverse denoising process, guided by the posterior distribution, allows for escaping from local minima, enabling the process to initiate from either white noise or any initial solution. Another enhancement is eliminating the feature backbone during the reverse denoising process at inference time. This streamlined design enables the denoising sampling process to explore a broader solution space (e.g., the matrix space), increasing diversity and facilitating more iterative steps. The findings from our empirical experiments support these claims.

Our contributions are summarized as follows:

- To our knowledge, we are the first to deploy the diffusion model in the doubly stochastic matrix space for iteratively exploring the optimal matching matrix through the reverse denoising sampling process.
- The lightweight design of our reverse denoising module results in faster convergence in the reverse sampling process. Moreover, our framework can effectively utilize reverse denoising sampling in a noise-to-target fashion or start from a highly reliable initial solution.
- We conducted comprehensive experiments on the real-world 4DMatch [30], 3DMatch [31], and RGB-D Scenes V2 [4], [31] datasets to validate the effectiveness of our diffusion matching model on 3D registration and 2D3D registration task.

## II. RELATED WORK

### A. 3D and 2D3D Registration

The registration problem estimates the transformation between the point cloud pair or the image-to-point-cloud pair. Recently, there have been significant advancements in feature learning-based methods for point cloud registration. Many of these state-of-the-art approaches, such as [3], [6], [11], [12], [32], [33], leverage a backbone architecture similar to KPConv [14] to downsample points and generate features with larger receptive fields. To further enhance the performance of these methods, they integrate prior knowledge and incorporate

learnable outlier rejection modules. For instance, GeoTR [6] introduces angle-wise and edge-wise embeddings into the transformer encoder, while RoITr [2] integrates local Point Pair Features (PPF) [34] to improve rotation invariance.

In addition to feature learning-based methods, another category of registration methods focuses on outlier rejection of candidate correspondences. For instance, PointDSC [17] utilizes a maximum clique algorithm in the local patch to cluster inlier correspondences. SC2-PCR [18] constructs a second-order consistency graph for candidate correspondences and theoretically demonstrates its robustness. Building on the second-order consistency graph proposed by SC2-PCR [18], MAC [20] introduces a variant of maximum clique algorithms to generate more reliable candidate inlier correspondences. Moreover, methods such as PEAL [33] and DiffusionPCR [35] employ an iterative refinement strategy to enhance the overlap prior information obtained from a pre-trained GeoTr [6].

Recently, significant advancements have been made in 2D3D registration methods [4], [36]–[38]. These methods face similar challenges to 3D registration tasks, with the additional complexity of scale inconsistency caused by the perspective projection of images. To address the issue of scale inconsistency, we propose the incorporation of a pre-trained feature backbone, DINO v2 [39], which offers superior multiscale features. Additionally, implementing diffused data augmentation in our diffusion matching model can enhance the ability to identify prominent combinational and consistent correspondences.

### B. Diffusion Models for 3D Registration

Recently, the diffusion model [23], [24], [40] has made great development in many fields, including human pose estimation [41], [42], camera pose estimation [43], object detection [44], segmentation [45], [46]. These developments have been achieved through a generative Markov Chain process based on the Langevin MCMC [47] or a reversed diffusion process [24]. Recognizing the power of the diffusion model to iteratively approximate target data distributions from white noise using hierarchical variational decoders, researchers have started applying it to point cloud registration and 6D pose estimation problems.

The pioneer work [48] that applied the diffusion model in the SE(3) space was accomplished by utilizing NCSN [40] to learn a denoising score matching function. This function was

then used for reverse sampling with Langevin MCMC in SE(3) space to evaluate 6DoF grasp pose generation. Additionally, [49] implemented DDPM [23] in the SE(3) space for 6D pose estimation by employing a surrogate point cloud registration baseline model. Similarly, GeoTR [6] served as a denoising module in [35], gradually denoising the overlap prior given by the pre-trained model, following a similar approach to PEAL [33].

### III. THE PROPOSED APPROACH

#### A. Problem Formulation

Given source point clouds  $P \in \mathbb{R}^{N \times 3}$  and target point clouds  $Q \in \mathbb{R}^{M \times 3}$ , the 3D registration task is to find top-k correspondences  $\mathcal{C}$  from matching matrix  $E$  and to conduct warping transformation ( $T \in SE(3)$  for rigid transformations, and 3D flow fields for non-rigid transformations) to align the overlap region of  $P$  and  $Q$ . In the context of 2D-3D registration, with a source image  $X \in \mathbb{R}^{H \times W \times 2}$  and target point cloud  $Q \in \mathbb{R}^{M \times 3}$ , the standard pipeline involves determining the top-k correspondences  $\mathcal{C} = \{(x_i, q_j) | x_i \in \mathbb{R}^2, q_j \in \mathbb{R}^3\}$ , and then estimating the rigid transformation  $T \in SE(3)$  by minimizing the 2D projection error:

$$\min_{T \in SE(3)} \sum_{x_i, q_j \in \mathcal{C}} \|Proj(T(q_j), K) - x_i\|_2$$

where  $K$  represents the camera intrinsic matrix, and  $Proj(\cdot, \cdot)$  denotes the projection function from 3D space to the image plane.

#### B. Preliminaries

**Revisiting Doubly Stochastic Matrix.** We can represent the point clouds  $P$  and  $Q$  as two graphs, denoted as  $\mathcal{G}_1 = \{P, E^P\}$  and  $\mathcal{G}_2 = \{Q, E^Q\}$ , where  $E^P$  and  $E^Q$  are respective edge sets. The matching matrix between these two graphs is a one-to-one mapping  $E \in \{0, 1\}^{N \times M}$ . In cases where  $N \neq M$  (e.g.,  $N > M$ ), we can introduce  $N - M$  dummy points in  $Q$  to make a square matching matrix, also known as a permutation matrix  $\mathcal{M} = \{A : A1_N = 1_N, A^T 1_N = 1_N, A \geq 0\}$ . Then, we further employ sinkhorn iterations [50] to convert this non-negative real matrix into a ‘‘doubly stochastic’’ matrix, which has uniform row sum  $M$  and column sum  $N$  [27].

In the registration tasks, the many-to-one relationship between the matching matrix space and the warping operation space serves as a motivation for us:

$$\begin{aligned} \min_{E \in \mathcal{M}} \sum_{i=1}^N \sum_{j=1}^M E_{ij} * \|W^E(p_i) - q_j\|_2 &\leq \\ \min_{W \in SE(3)/\mathbb{R}^{3N}/\mathbb{R}^{2N}} \sum_{i=1}^N \sum_{j=1}^M \hat{E}_{ij}^W * \|W(p_i) - q_j\|_2 & \end{aligned}$$

where  $W^E$  is a warping generated by  $E$  and  $\hat{E}^W$  is a matching matrix computed by the warping  $W$ .

#### C. Overview

Our framework comprises a feature backbone (e.g., KPConv [14] or ResNet [15]) and a diffusion matching model [23]. In the 3D registration task, the KPConv backbone takes source point clouds  $P$  and target  $Q$  as input and performs downsamplings to obtain the superpoints  $\hat{P}$  and  $\hat{Q}$ , along with their associated features  $F^{\hat{P}} \in \mathbb{R}^{N \times d}$  and  $F^{\hat{Q}} \in \mathbb{R}^{M \times d}$ . In the 2D3D registration task, a ResNet [15] with FPN [51] downsamples the image  $X \in \mathbb{R}^{H \times W \times 2}$  (in image-point-coud pair  $(X, Q)$ ) to the superpixels  $\hat{X} \in \mathbb{R}^{\hat{H} \times \hat{W} \times 2}$  and give the associated image feature  $F^{\hat{X}} \in \mathbb{R}^{\hat{H} \times \hat{W} \times d}$ , while the target point cloud  $Q$  is processed by a KPConv backbone, similar to the 3D registration task. Additionally, a depth map  $D^{\hat{X}}$  and new superpixel feature  $F_{dino}^{\hat{X}}$  for superpixels  $\hat{X}$  are given by the pre-trained depth estimation model [52] and visual feature backbone DINO v2 [39], respectively.

Our diffusion module  $g_\theta$  (refer to section III-E) takes these superpoints (or superpixels) and associated features as inputs. We employ one loss for our denoising module and another for the single-pass prediction head by leveraging the backbone features for supervision during joint training. During inference, we utilize  $g_\theta$  in the reverse sampling process to predict the target matching matrix  $E^0$  from any noisy one and apply DDIM [24] in the reverse sampling process to sample a more accurate matching matrix. The denoising module  $g_\theta$  primarily consists of four key components: (1) Sinkhorn Projection [50], (2) Weighted SVD [53], (3) Denoising Transformer Network [54] and (4) Matching function.

#### D. Diffusion Model in Doubly Stochastic Matrix space

In this section, we introduce the construction of our diffusion matching model for generating the matching matrix between two scans. We denote the matching matrix as  $E \in \{0, 1\}^{N \times M}$ , and we assume  $E$  is defined in a nonsquare ‘‘doubly stochastic’’ matrix space  $\mathcal{M}$ .

**Forward Diffusion Process.** As mentioned in DDPM [23], the forward diffusion process is fixed to a Markovian chain, denoted as  $q(E^{1:T} | E^0)$ , which generates a sequence of latent variables  $E^t$  by gradually injecting Gaussian noise into the ground truth matching matrix  $E^0$ . The diffused matching matrix  $E^t$  at arbitrary timestep  $t$  has a closed form:

$$E^t \sim q(E^t | E^0) = N(E^t; \sqrt{\alpha} E^0, (1 - \bar{\alpha}) \mathbf{I}). \quad (1)$$

where the added noise over each element of the matrix is sampled independently and identically distributed (i.i.d.). However, this diffused  $E^t \sim q(E^t | E^0)$  is a continuous matrix in  $\mathbb{R}^{N \times M}$ , which is outside the feasible solution space of matching matrices (i.e., doubly stochastic matrix manifolds). To address this issue, we apply the following projection to confine the matrix  $E^t$  to the feasible solution space  $\mathcal{M}$ :

$$\begin{aligned} (\text{Rigid}) \mathbf{E}^t &= \sqrt{\bar{\alpha}_t} \mathbf{E}^0 + \sqrt{1 - \bar{\alpha}_t} f_\epsilon(\epsilon_0), \tilde{\mathbf{E}}^t = \mathbf{E}^t - \text{Min}(\mathbf{E}^t), \\ (\text{Deformable}) \mathbf{E}^t &= \sqrt{\bar{\alpha}_t} \mathbf{E}^0 + \sqrt{1 - \bar{\alpha}_t} \epsilon_0, \tilde{\mathbf{E}}^t = \text{Sigmoid}(\mathbf{E}^t), \\ \hat{\mathbf{E}}^t &= \mathbf{f}_{\text{sinkhorn}}(\tilde{\mathbf{E}}^t) \end{aligned} \quad (2)$$

where the  $\mathbf{f}_{\text{sinkhorn}}$  operation is from the Sinkhorn algorithm [50] and  $f_\epsilon = (\epsilon \% 1)(\text{abs}(\epsilon)/\epsilon)\eta$ . We empirically set  $\eta = 1.5$  and  $\epsilon_0 \sim \mathcal{N}(\epsilon; 0, \mathbf{I})$ .

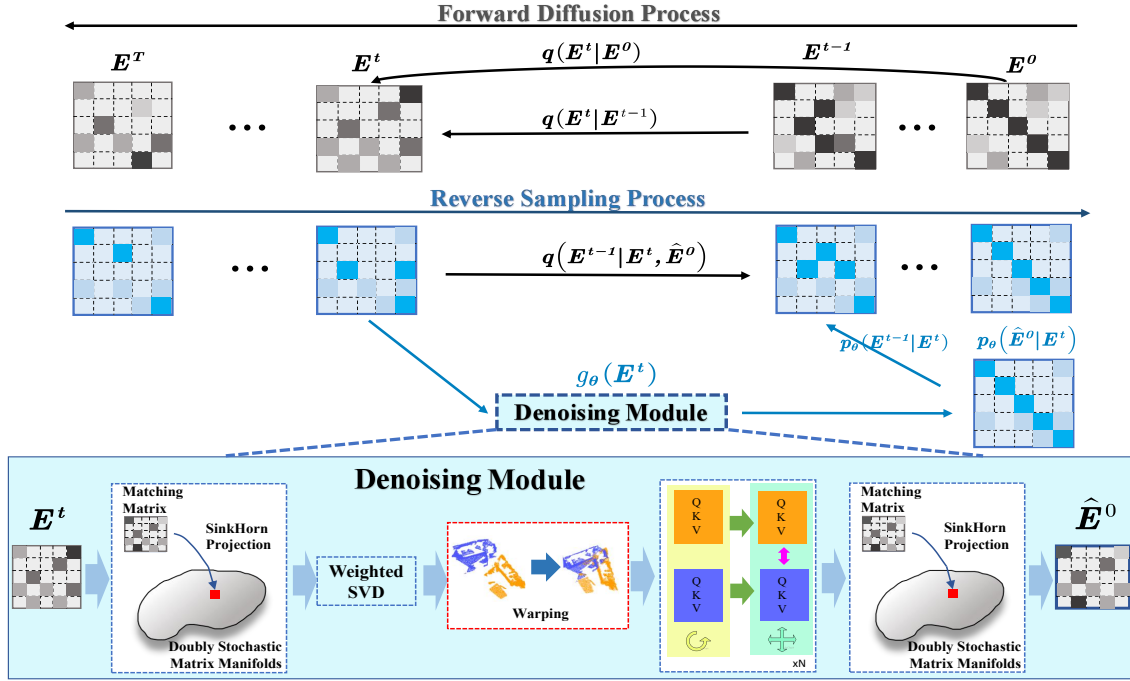


Fig. 2. Overview of our diffusion matching model. The forward diffusion process is driven by the Gaussian transition kernel  $q(E^t|E^{t-1})$ , which has a closed form  $q(E^t|E^0)$ . The denoising model  $g_\theta(E^t)$  learns a reverse denoising gradient that points to the target solution  $E^0$ . During inference in the reverse sampling process, we utilize the predicted  $\hat{E}_0$  and DDIM. ([24]) to sampling  $E^{t-1}$ .

**Reverse Denoising Sampling Process.** Given a diffusion Markovian chain  $E^0 \rightarrow E^1 \rightarrow \dots \rightarrow E^T$ , we need to learn a reverse transition kernel with the posterior distribution  $q(E^{t-1}|E^t, E^0)$  to sample the reverse Markovian chain  $E^T \rightarrow E^{T-1} \rightarrow \dots \rightarrow E^0$  from a white noise  $E^T$  to achieve the target matching matrix. The posterior distribution  $q(E^{t-1}|E^t, E^0)$  conditioned on  $E^0$  and  $E^t$  is defined as:

$$\begin{aligned} q(E^{t-1}|E^t, E^0) &= \frac{q(E^t|E^{t-1}, E^0)q(E^{t-1}|E^0)}{q(E^t|E^0)} \\ &\propto N(E^{t-1}; \underbrace{\sqrt{\alpha_t}(1 - \bar{\alpha}_{t-1})E^t + \sqrt{\bar{\alpha}_{t-1}}(1 - \alpha_t)E^0}_{\mu_q(E^t, E^0)}, \underbrace{\frac{(1 - \alpha_t)(1 - \bar{\alpha}_{t-1})}{1 - \bar{\alpha}_t}}_{\Sigma_q(t)} \mathbf{I}). \end{aligned} \quad (3)$$

For latent variable  $E^{1:T}$ , the Evidence Lower Bound (ELBO) for  $E^0$  with distribution  $q$  formulates as:

$$\begin{aligned} &\log(p_\theta(E^0)) \\ &\geq \mathbb{E}_{q(E^{1:T}|E^0)} \left[ \log \left( \frac{p_\theta(E^{0:T})}{q(E^{1:T}|E^0)} \right) \right] = L_{vb}(E^0) \\ &= \mathbb{E}_{q(E^1|E^0)} [\log(p_\theta(E^0|E^1))] + \mathbb{E}_{q(E^T|E^0)} \left[ \log \left( \frac{p_\theta(E^T)}{q(E^T|E^0)} \right) \right] \\ &+ \sum_{t=2}^T \mathbb{E}_{q(E^t, E^{t-1}|E^0)} \left[ \frac{p_\theta(E^{t-1}|E^t)}{q(E^{t-1}|E^t, E^0)} \right] \\ &= C_\theta(E^T, E^1, E^0) \\ &- \sum_{t=2}^T \underbrace{\mathbb{E}_{q(E^t|E^0)} [D_{KL}(q(E^{t-1}|E^t, E^0)||p_\theta(E^{t-1}|E^t))]}_{\text{denoising matching term}}. \end{aligned}$$

Since we propose a lightweight denoising network  $g_\theta(E^t)$  seek to predict  $E^0$  from any noisy one  $E^t$ , the ELBO can be simplified to:

$$\begin{aligned} &\arg \min_{\theta} D_{KL}(q(E^{t-1}|E^t, E^0)||p_\theta(E^{t-1}|E^t)) \\ &= \arg \min_{\theta} D_{KL}(\mathcal{N}(E^{t-1}, \mu_q, \Sigma_q(t))||\mathcal{N}(E^{t-1}, \mu_\theta, \Sigma_\theta(t))) \\ &= \arg \min_{\theta} \frac{1}{2\sigma_q^2(t)} \frac{\bar{\alpha}(1 - \alpha_t)^2}{(1 - \bar{\alpha})^2} \left[ \|g_\theta(E^t) - E^0\|_2^2 \right] \\ &\equiv - \arg \min_{\theta} \mathbb{E}_{q(E^0)} [\mathbb{E}_{q(E^t|E^0)} \log p_\theta(E^0|E^t)] \end{aligned} \quad (4)$$

where  $\sigma_q^2(t) = \frac{(1 - \alpha_t)(1 - \bar{\alpha}_{t-1})}{1 - \bar{\alpha}}$ .

Based on the derivation of Eqn. (4), we can utilize the following simplified version loss to train  $p_\theta(E^0|E^t)$ :

$$\begin{aligned} L_{simple} &= \\ &- \mathbb{E}_{q(E^0)} \left[ \sum_{t=1}^T \left( \frac{T - t + 1}{T} \right) \mathbb{E}_{q(E^t|E^0)} \log p_\theta(E^0|E^t) \right], \end{aligned} \quad (5)$$

where the reweighting term  $\frac{T-t+1}{T}$  implies that the loss at time steps closer to  $T$  is weighted less than at earlier steps.

### E. The Lightweight Denoising Module $g_\theta$

This section outlines the architecture of the lightweight denoising module  $g_\theta$ . In 3D registration tasks, we take the downsampled superpoints  $\hat{P}$  and  $\hat{Q}$  along with the points features  $F^{\hat{P}}$  and  $F^{\hat{Q}}$  as the inputs of  $g_\theta$  in each reverse sampling step. Similarly, in 2D3D registration tasks, the inputs of  $g_\theta$  are downsampled superpixels  $\hat{X}$  and  $\hat{Q}$  with associated inputs  $\{F^{\hat{X}}, D^{\hat{X}}, F_{dino}^{\hat{X}}, F^{\hat{Q}}\}$ . When inference,  $g_\theta$  inputs a noised matching matrix  $E^t$  and outputs a predicted target matching matrix  $\hat{E}_0$ .

We define the denoising module  $g_\theta$  by sequentially stacking five components as a differentiable layer: SinkHorn Projection, Weighted SVD, Warping Function, Denoising Transformer, and Matching function. The Weighted SVD operation can be viewed as a differentiable projection that arises from the matching matrix obtained from the first Sinkhorn Projection. Alternatively, in the context of a 2D-3D registration task, this Weighted SVD operation can be substituted with a differentiable PnP (Perspective-n-Point) solver [55].

**Sinkhorn Projection:**  $\mathbf{f}_{\text{sinkhorn}}(\cdot)$ . To constrain the matching matrix  $E^t$  within the doubly stochastic matrices manifolds, we utilize the SinkHorn [50] iterations to project  $E^t$ . We treat this operation as a key role in our framework rather than a post-processing in other methods.

**Weighted SVD:**  $\text{soft\_procrustes}(\cdot, \cdot, \cdot)$ . Given top-k confident correspondences  $K$ , we utilize the weighted SVD algorithm [56] (differentiable) to compute the transformation  $R, t$  in a closed form:

$$\begin{aligned} H &= \sum_{(i,j) \in C} \tilde{E}(i,j) \hat{p}_i \hat{q}_j^T, \quad H = U \Sigma V^T \\ \mathbf{R} &= \text{Udiag}(1, 1, \det(UV^T))V, \\ \mathbf{t} &= \frac{1}{|K|} \left( \sum_{(i,\cdot) \in K} \hat{p}_i - \mathbf{R} \sum_{(\cdot,j) \in K} \hat{q}_j \right) \end{aligned} \quad (6)$$

where  $(\hat{p}_i, \hat{q}_j)$  is a superpoint correspondences. In the 2D3D registration task, we first project a superpixel depth map  $D^{\hat{X}}$  to a point cloud  $P_D^{\hat{X}}$  using camera intrinsic. Then we utilize this SVD decomposition to compute  $\mathbf{R}, \mathbf{t}$  with  $P_D^{\hat{X}}$  and  $\hat{Q}$  as inputs.

**Warping Function:**  $\text{warping}(\cdot, \cdot, \cdot)$ . After obtaining transformation  $\mathbf{R}, \mathbf{t}$ , the rigid warping of source point clouds is computed by  $W(\hat{p}_i) = \mathbf{R}\hat{p}_i + \mathbf{t}$ . In this paper, we use rigid warping for rigid and deformable registration cases to demonstrate our design. As for deformable registration, with the denoised correspondences, we can compute the flow fields for all points in  $\hat{P}$  by performing nearest neighbor interpolation with the predicted inlier correspondences as anchors. For the deformation warping, we actually can build a deformation graph [57], [58] to conduct deformable warping [30], [59] for the source point cloud  $\hat{P}$ . We leave this deformable warping integration in future work.

**Denoising Transformer:**  $f_\theta(\cdot, \cdot, \cdot, \cdot, \cdot, \cdot)$ . We observed empirically that a simple noise model does not hurt performance. Thus, we exploit a lightweight Transformer [54] as our denoising network. Specifically, we utilize a 6-layer interleaved attention layers transformer  $f_\theta$  for denoising feature embedding.

**Attention layer.** In the 3D registration task, following [8], the  $q, k, v$  in the self-attention, are computed as:

$$\begin{aligned} q_i &= \Theta(p_i) \mathbf{W}_q f^{\hat{p}_i}, \quad k_j = \Theta(p_j) \mathbf{W}_k f^{\hat{p}_j}, \quad v_j = \mathbf{W}_v f^{\hat{p}_j}, \\ f^{\hat{p}_i} &= f^{\hat{p}_i} + \text{MLP}(\text{cat}[f^{\hat{p}_i}, \sum_j \alpha_{ij} v_j]), \end{aligned} \quad (7)$$

where  $\mathbf{W}_q, \mathbf{W}_k, \mathbf{W}_v \in \mathbb{R}^{d \times d}$  are the attention weights,  $\alpha_{ij} = \text{softmax}(q_i k_j^T / \sqrt{d})$ , and  $\Theta(\cdot)$  is a rotary position

encoding [8].  $\text{MLP}(\cdot)$  is a 3-layer fully connected network, and  $\text{cat}[\cdot, \cdot]$  is the concatenating operator. The cross attention layer is the standard form that  $q$  and  $k, v$  are computed by source and target point clouds, respectively. Other operations are the same with self-attention. In the 2D3D registration task, we take image inputs  $\{\hat{X}, F^{\hat{X}}, F_{\text{dino}}^{\hat{X}}\}$  and point cloud input  $\{\hat{Q}, F^{\hat{Q}}\}$  to compute  $q, k, v$  by utilizing standard attention layers [54]. We also take Fourier embedding function [60] to embed superpixels  $\hat{X}$  and superpoints  $\hat{Q}$  as positional encoding.

**Matching function:**  $\text{matching\_logits}(\cdot, \cdot, \cdot, \cdot)$ . We compute matching ‘‘logits’’ between  $\hat{P}$  and  $\hat{Q}$  by features  $F^{\hat{P}}$  (or  $F^{\hat{X}}$ ) and  $F^{\hat{Q}}$ :  $\tilde{E}(i, j) = \frac{1}{\sqrt{d}} \langle f^{\hat{p}_i}, f^{\hat{q}_j} \rangle$ .

For the sake of clarity, we provide pseudo-code in Algorithm.1 to describe the logic of our entire denoising module  $g_\theta$  for the 3D Registration task. The definition of  $g_\theta$  for the 2D3D registration task is similar, which can be found in section (IV-B), Algorithm.4, and Algorithm.5.

---

**Algorithm 1** Denoising Module  $g_\theta$  for 3D Registration Task.

**Require:** Sampled matching matrix  $\mathbf{E}^t \in \mathbb{R}^{N \times M}$ ; Point clouds  $\hat{P}, \hat{Q} \in \mathbb{R}^3$  and associated point features  $\mathbf{F}^{\hat{P}}, \mathbf{F}^{\hat{Q}}$ .

**Ensure:** Target matching matrix  $\tilde{\mathbf{E}}_0$ .

```

1: function  $g_\theta(\mathbf{E}^t, \hat{P}, \hat{Q}, \mathbf{F}^{\hat{P}}, \mathbf{F}^{\hat{Q}})$ 
2:    $\tilde{\mathbf{E}}_t \leftarrow \mathbf{f}_{\text{sinkhorn}}(\mathbf{E}^t)$ 
3:    $\hat{\mathbf{R}}_t, \hat{\mathbf{t}}_t \leftarrow \text{soft\_procrustes}(\tilde{\mathbf{E}}_t, \hat{P}, \hat{Q}), \hat{P}_t \leftarrow$ 
      $\text{warping}(\hat{P}, \hat{\mathbf{R}}_t, \hat{\mathbf{t}}_t)$ 
4:    $\tilde{\mathbf{F}}^{\hat{P}_t}, \tilde{\mathbf{F}}^{\hat{Q}_t} \leftarrow f_\theta(\hat{P}_t, \hat{Q}, \mathbf{F}^{\hat{P}}, \mathbf{F}^{\hat{Q}}, \Theta(\hat{P}_t), \Theta(\hat{Q}))$ 
5:    $\tilde{\mathbf{E}}_0 \leftarrow \text{matching\_logits}(\tilde{\mathbf{F}}^{\hat{P}_t}, \tilde{\mathbf{F}}^{\hat{Q}_t}, \Theta(\hat{P}_t), \Theta(\hat{Q}))$ 
6:    $\hat{\mathbf{E}}_0 \leftarrow \mathbf{f}_{\text{sinkhorn}}(\tilde{\mathbf{E}}_0)$ 
7:   return  $\hat{\mathbf{E}}_0$ 
8: end function
```

---

## IV. EXPERIMENTS

In this section, we conduct experiments on 3D registration and 2D3D registration tasks to prove the effectiveness of our method.

---

**Algorithm 2** Training Diff-Reg in 3D Registration Task

**Require:** Point clouds  $\hat{P}, \hat{Q} \in \mathbb{R}^3$  and associated point features  $\mathbf{F}^{\hat{P}}, \mathbf{F}^{\hat{Q}}$ .

```

1: while not converged do
2:   Sample  $\mathbf{E}^0 \sim q(\mathbf{E}^0)$ 
3:    $N \times M \leftarrow \mathbf{E}^0.\text{shape}$ 
4:   Sample  $t \sim \text{Uniform}(1, \dots, T)$ 
5:    $\epsilon \sim \mathcal{N}(0, 1)^{N \times M}$ 
6:   if Rigid then
7:      $\mathbf{E}^t \leftarrow \sqrt{\bar{\alpha}_t} \mathbf{E}^0 + \sqrt{1 - \bar{\alpha}_t} f_\epsilon(\epsilon), \tilde{\mathbf{E}}^t = \mathbf{E}^t -$ 
        $\text{Min}(\mathbf{E}^t)$ 
8:   else
9:      $\mathbf{E}^t = \sqrt{\bar{\alpha}_t} \mathbf{E}^0 + \sqrt{1 - \bar{\alpha}_t} \epsilon_0, \tilde{\mathbf{E}}^t = \text{Sigmoid}(\mathbf{E}^t)$ 
10:  end if
11:   $\hat{\mathbf{E}}_0 \leftarrow g_\theta(\tilde{\mathbf{E}}^t, \hat{P}, \hat{Q}, \mathbf{F}^{\hat{P}}, \mathbf{F}^{\hat{Q}})$ 
12:  Optimize  $L_t = \text{Focal\_loss}(\hat{\mathbf{E}}_0, \mathbf{E}^0)$ 
13: end while
```

---

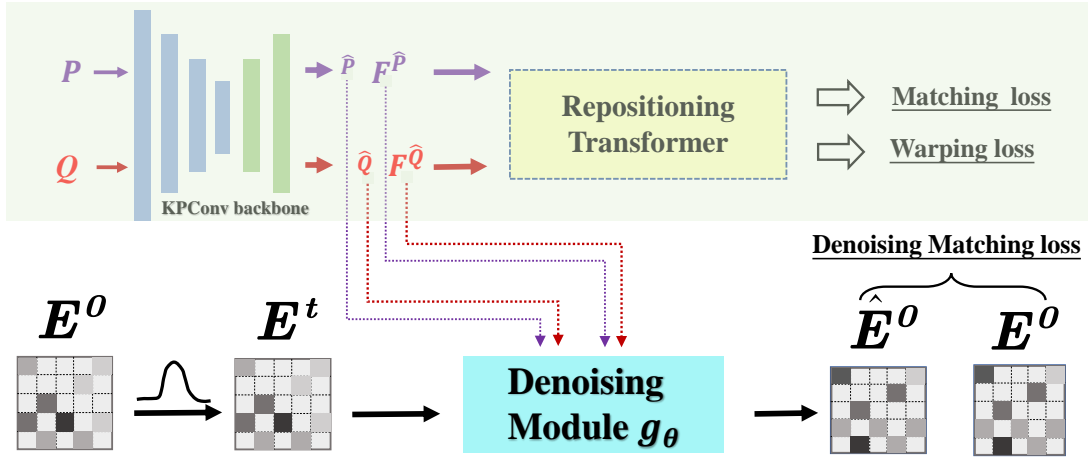


Fig. 3. Overview of our diffusion matching model in 3D registration task. The top half is the **single-pass prediction head** with the feature backbone, while the bottom is our denoising module.

---

**Algorithm 3** Sampling by Diff-Reg in 3D Registration Task

**Require:** Initial matching matrix  $E^T$  from backbone or white noise; Point clouds  $\hat{P}, \hat{Q} \in \mathbb{R}^3$  and associated point features  $F^{\hat{P}}, F^{\hat{Q}}$ .

**Ensure:** Target matching matrix  $\tilde{E}^0$ .

```

1:  $N \times M \leftarrow E^T.shape$ 
2: for  $t = T, \dots, 1$  do
3:    $z_t \sim N(0, 1)^{N \times M}$  if  $t > 1$  else  $z_t \leftarrow \mathbf{0}^{N \times M}$ 
4:   if Rigid then
5:      $\hat{E}^t = E^t - \text{Min}(E^t)$ 
6:   end if
7:    $\hat{E}_0 \leftarrow g_\theta(\hat{E}^t, \hat{P}, \hat{Q}, F^{\hat{P}}, F^{\hat{Q}})$ 
8:    $\epsilon_t \leftarrow \frac{\hat{E}_0}{\sqrt{1-\alpha_t}} - \frac{\sqrt{\alpha_t}}{\sqrt{1-\alpha_t}} \hat{E}^t$ 
9:    $\sigma_t \leftarrow \sqrt{\frac{(1-\alpha_{t-1})}{1-\alpha_t}} \sqrt{1 - \frac{\alpha_t}{\alpha_{t-1}}}$ 
10:   $\hat{E}^{t-1} \leftarrow \sqrt{\alpha_{t-1}} \hat{E}_0 + \sqrt{1 - \alpha_{t-1} - \sigma_t^2} \epsilon_t + \sigma_t z_t$ 
11: end for
12: if Rigid then
13:    $\tilde{E}^0 = \hat{E}^0 - \text{Min}(\hat{E}^0)$ ,  $\tilde{E}^0 = \mathbf{f}_{\text{sinkhorn}}(\tilde{E}^0)$ 
14: else
15:    $\tilde{E}^0 = \text{Sigmoid}(\hat{E}^0)$ 
16: end if
    
```

---

### A. 3d Registration Task

1) **Implementation Details.**: The training of our 3D registration network architecture is shown in Fig. 3. We utilize the joint training strategy for the single-pass prediction head and our denoising module. Our framework utilize a KPConv [14] branch to give the downsampled the superpoints  $\hat{P}$  and  $\hat{Q}$  and the associated features  $F^{\hat{P}}$  and  $F^{\hat{Q}}$ . Subsequently, we employ a repositioning transformer [8] to provide a single-pass prediction of the matching matrix and the resulting transformation  $R, t$  both of which are supervised by the Matching loss  $L_M$  and Warping loss  $L_W$  introduced in [8]. We utilize the focal loss  $L_{\text{simple}}$  (Eqn.5) to guide the training of the denoising module  $g_\theta$ . The total loss function is defined as  $L = L_M + L_W + L_{\text{simple}}$ . During inference, we use the feature

backbone to generate the superpoint features  $F^{\hat{P}}$  and  $F^{\hat{Q}}$  and treat them as constant frozen features in the reverse denoising sampling process. The dimension  $d$  of superpoint features  $F^{\hat{P}}$  and  $F^{\hat{Q}}$  is set as  $d = 528$ . The training and reverse sampling of denoising module  $g_\theta$  are in Algorithm. 2 and Algorithm. 3.

Our proposed model is trained and evaluated using PyTorch on an NVIDIA RTX 3090 GPU. We train the model for approximately 30 epochs on the 3DMatch and 4DMatch datasets with a batch size of 2. We adopt the training/validation/test split strategy from [8], [11] for 3DMatch and 4DMatch datasets. The total diffusion steps during training are set to 1000.

#### 2) Non-Rigid 4DMatch/4DLoMatch Benchmark.:

a) **Datasets.**: 4DMatch/4DLoMatch [8] is a benchmark generated by the animation sequences from Deforming Things4D [61]. We follow the dataset split provided in [8], which has a wide range of overlap ratio, that 45%-92% in 4DMatch and 15%-45% in 4DLoMatch.

b) **Metrics.**: Following Leopard [8], we utilize two evaluation metrics to assess the quality of predicted matches. (1) Inlier ratio (**IR**): This metric represents the correct fraction in the correspondences prediction  $\mathcal{K}_{\text{pred}}$ . (2) Non-rigid Feature Matching Recall (**NFMR**): This metric calculates the fraction of ground truth correspondences  $(u, v) \in \mathcal{K}_{\text{gt}}$  that can be successfully recovered by using the predicted correspondences  $\mathcal{K}_{\text{pred}}$  as anchors. The NFMR metric provides a better characterization of the global rationality of overall body deformation, directly indicating whether the anchor  $\mathcal{K}_{\text{pred}}$  effectively captures the body movements.

Specifically, **IR** measure denotes the correct fraction in the correspondences prediction  $\mathcal{K}_{\text{pred}}$ :

$$IR = \frac{1}{|\mathcal{K}_{\text{pred}}|} \sum_{(p,q) \in \mathcal{K}_{\text{pred}}} [\|W_{\text{gt}}(p) - q\|_2 < \sigma] \quad (8)$$

where  $\|\cdot\|_2$  is the Euclidean norm,  $W_{\text{gt}}(\cdot)$  is the ground truth warping function,  $[\cdot]$  is the Inverse bracket, and  $\sigma = 0.04m$ . The **NFMR** metric is to compute the fraction of the ground truth correspondences  $(u, v) \in \mathcal{K}_{\text{gt}}$  that can be successfully recovered from the predicted correspondences  $\mathcal{K}_{\text{pred}}$ . First,

we construct the predicted correspondences  $\mathcal{A} = \{p|(p, q) \in \mathcal{K}_{pred}\}$  and the associated sparse 3D flow fields  $\mathcal{F} = \{q - p|(p, q) \in \mathcal{K}_{pred}\}$ . Then, for any source point  $u$  in  $\mathcal{K}_{gt}$ , we can recover the flow field for  $u$  by inverse distance interpolation:

$$\Gamma(u, \mathcal{A}, \mathcal{F}) = \frac{\sum_{\mathcal{A}_i \in \mathcal{N}(u, \mathcal{A})} \mathcal{F}_i \|u - \mathcal{A}_i\|_2^{-1}}{\sum_{\mathcal{A}_i \in \mathcal{N}(u, \mathcal{A})} \|u - \mathcal{A}_i\|_2^{-1}} \quad (9)$$

where  $\mathcal{N}(\cdot, \cdot)$  is k-nearest neighbors search with  $k = 3$ . After that, we define the *NFMR* to measure the fraction of ground truth matches that we recovered from  $\mathcal{K}_{pred}$ :

$$NFMR = \frac{1}{|\mathcal{K}_{gt}|} \left| \left| \Gamma(u, \mathcal{A}, \mathcal{F}) - (v - u) \right|_2 < \sigma \right| \quad (10)$$

*c) Quantitative results.:* We compare our method with two categories of state-of-the-art methods. The first category includes Scene Flow Methods such as PWC [62], FLOT [63], and NSFP [64]. The second category encapsulates Feature Matching-Based Methods, namely D3Feat [3], Predator [11], Leopard [8], GeoTR [6], and RoITr [2]. As illustrated in Table I, our method demonstrates significant improvements compared to the single-pass baselines. “Diff-Reg(Backbone)” refers to the single-pass prediction head (i.e., reposition transformer in Leopard [8]), while “Diff-Reg(Diffusion/1)” and “Diff-Reg(Diffusion/20)” utilize our denoising module  $g_\theta$  with one single step and 20 steps of reverse denoising sampling. For both NFMR and IR metrics, “Diff-Reg(Diffusion/20)” achieves the best performance. The improvement in NFMR of “Diff-Reg(Backbone)” compared to the baselines indicates that our diffused training samples in the matching matrix space enhance the feature backbone’s representation, enabling the capture of crucial salient correspondences that are helpful for consistent global deformation. The significant enhancement of “Diff-Reg(Diffusion/20)” over “Diff-Reg(Diffusion/1)” demonstrates that the reverse denoising sampling process indeed searches for a better solution guided by the learned posterior distribution. To validate that the predicted correspondences indeed improve deformable registration, we conducted experiments using the state-of-the-art registration method GraphSCNet [59]. As indicated in Table II, our predicted correspondences are beneficial for deformable registration, particularly in the more challenging 4DLoMatch benchmark.

*d) Qualitative results.:* We provide a visualization to demonstrate our method’s effectiveness in Fig.4. For a fair comparison, we exploit the “metric index” (i.e., the test point set in the 4DMatch/4DLoMatch dataset, in blue color) of the source point cloud for all methods. Taking the predicted correspondences from RoITr [2], GeoTr [2], and “Our (Diffusion/20)” as anchor correspondences, we calculate the deformation flow for the source test points by applying neighborhood k-nearest neighbors (knn) interpolation based on the anchors. The deformable registration of the bear’s two front paws in the first row and fourth column reveals that dealing with ambiguous matching patches of asymmetric objects can be highly challenging. However, our denoising process is capable of handling this scenario perfectly. The deformable registration results from the top three rows (from

the 4DMatch benchmark) indicate that the baseline methods struggle to compute reliable and consistent correspondences between scans with large deformations. The bottom two rows (from the 4DLoMatch benchmark) also demonstrate that low overlapping combined with deformation results in a disaster. These visualizations demonstrate that our denoising module in the matching matrix space may provide a more effective approach for tackling these challenges. We provide more additional visualizations about tough cases in Fig.7. The top three lines (in Fig.7) are from 4DMatch, while the bottom three lines are from the 4DLoMatch dataset. The results in the bottom three lines demonstrate that our denoising module can effectively handle scenes with “large deformations + low overlap,” whereas the top three lines show that our method excels in registering asymmetric objects.

### 3) Rigid 3DMatch/3DLoMatch benchmark.:

*a) Datasets.:* 3DMatch [31] is an indoor benchmark for 3D matching and registration. Following [6], [8], [11], we split it to 46/8/8 scenes for training/validation/testing. The overlap ratio between scan pairs in 3DMatch/3DLoMatch is about  $> 30\%/10\% - 30\%$ .

*b) Metrics.:* Following [6], [11], [66], we utilize three evaluation metrics to evaluate our method and other baselines: (1) Inlier Ratio (IR): The proportion of accurate correspondences in which the distance falls below a threshold (i.e.,  $0.1m$ ) based on the ground truth transformation. (2) Feature Matching Recall (FMR): The percentage of matched pairs that have an inlier ratio exceeding a specified threshold (i.e., 5%). (3) Registration Recall (RR): The fraction of successfully registered point cloud pairs with a predicted transformation error below a certain threshold (e.g.,  $RMSE < 0.2$ ).

*c) Results.:* We compared our method with some state-of-the-art feature matching based methods: FCGF [65], D3Feat [3], Predator [11], Leopard [8], GeoTr [6], and RoITr [2]. Diff-Reg(diffusion/1) and Diff-Reg(diffusion/20) represent our denoising module with one or twenty reverse sampling steps, respectively. As demonstrated in Table III, our method Diff-Reg(diffusion/20) achieves the highest registration recall on the 3DMatch benchmark.

TABLE I  
QUANTITATIVE RESULTS ON THE 4DMATCH AND 4DLOMATCH BENCHMARKS. THE BEST RESULTS ARE HIGHLIGHTED IN BOLD, AND THE SECOND-BEST RESULTS ARE UNDERLINED.

Category	Method	4DMatch		4DLoMatch	
		NFMR $\uparrow$	IR $\uparrow$	NFMR $\uparrow$	IR $\uparrow$
Scene Flow	PointPWC [62]	21.60	20.0	10.0	7.20
	FLOT [63]	27.10	24.90	15.20	10.70
Feature Matching	D3Feat [3]	55.50	54.70	27.40	21.50
	Predator [11]	56.40	60.40	32.10	27.50
	Lepard [8]	83.60	82.64	66.63	55.55
	GeoTR [6]	83.20	82.20	65.40	63.60
	RoITr [2]	83.00	<u>84.40</u>	69.40	<u>67.60</u>
	Diff-Reg(Backbone)	<u>85.47</u>	<u>81.15</u>	72.37	59.50
	Diff-Reg(Diffusion/1)	85.23	83.85	<u>73.19</u>	65.26
	Diff-Reg(Diffusion/20)	<b>88.40</b>	<b>86.41</b>	<b>76.23</b>	<b>67.80</b>

TABLE II  
NON-RIGID REGISTRATION RESULTS OF 4DMATCH/4DLOMATCH. GIVEN PREDICTED CORRESPONDENCES, WE UTILIZE THE NON-RIGID REGISTRATION METHOD GRAPHSCNET [59] TO CONDUCT THE DEFORMABLE REGISTRATION. WE RETRAIN RoITR\* USING THE AUTHORS' CODE.

Method	4DMatch-F				4DLoMatch-F			
	EPE $\downarrow$	AccS $\uparrow$	AccR $\uparrow$	Outlier $\downarrow$	EPE $\downarrow$	AccS $\uparrow$	AccR $\uparrow$	Outlier $\downarrow$
PointPWC [62]	0.182	6.25	21.49	52.07	0.279	1.69	8.15	55.70
FLOT [63]	0.133	7.66	27.15	40.49	0.210	2.73	13.08	42.51
GeomFmaps [9]	0.152	12.34	32.56	37.90	0.148	1.85	6.51	64.63
Synorim-pw [19]	0.099	22.91	49.86	26.01	0.170	10.55	30.17	31.12
Lepard [8]+GraphSCNet [59]	<u>0.042</u>	70.10	83.80	<u>9.20</u>	<u>0.102</u>	<u>40.00</u>	<u>59.10</u>	<u>17.50</u>
GeoTR [6]+GraphSCNet [59]	0.043	<u>72.10</u>	<u>84.30</u>	9.50	0.119	41.00	58.40	20.60
RoITr* [2] +GraphSCNet [59]	0.056	59.60	80.50	12.50	0.118	32.30	56.70	20.50
Diff-Reg+GraphSCNet [59]	<b>0.041</b>	<b>73.20</b>	<b>85.80</b>	<b>8.30</b>	<b>0.095</b>	<b>43.80</b>	<b>62.90</b>	<b>15.50</b>

TABLE III  
QUANTITATIVE RESULTS ON THE 3DMATCH AND 3DLOMATCH BENCHMARKS. THE BEST RESULTS ARE HIGHLIGHTED IN BOLD, AND THE SECOND-BEST RESULTS ARE UNDERLINED.

Method	Reference	3DMatch			3DLoMatch		
		FMR $\uparrow$	IR $\uparrow$	RR $\uparrow$	FMR $\uparrow$	IR $\uparrow$	RR $\uparrow$
FCGF	ICCV2019 [65]	95.20	56.90	88.20	60.90	21.40	45.80
D3Feat	CVPR2020 [3]	95.80	39.00	85.80	69.30	13.20	40.20
Predator	CVPR2021 [11]	96.70	58.00	91.80	78.60	26.70	62.40
Lepard	CVPR2022 [8]	97.95	57.61	93.90	84.22	27.83	70.63
GeoTR	CVPR2022 [6]	<b>98.1</b>	72.7	92.3	<u>88.7</u>	<u>44.7</u>	75.4
RoITr	CVPR2023 [2]	<u>98.0</u>	<b>82.6</b>	91.9	<b>89.6</b>	<b>54.3</b>	74.8
PEAL-3D	CVPR2023 [33]	98.5	73.3	94.2	87.6	49.0	<u>79.0</u>
Diff-Reg(diffusion/1)		96.28	30.92	94.8	69.6	9.6	73.3
Diff-Reg(diffusion/20)		96.28	30.92	<b>95.0</b>	69.6	9.6	73.8

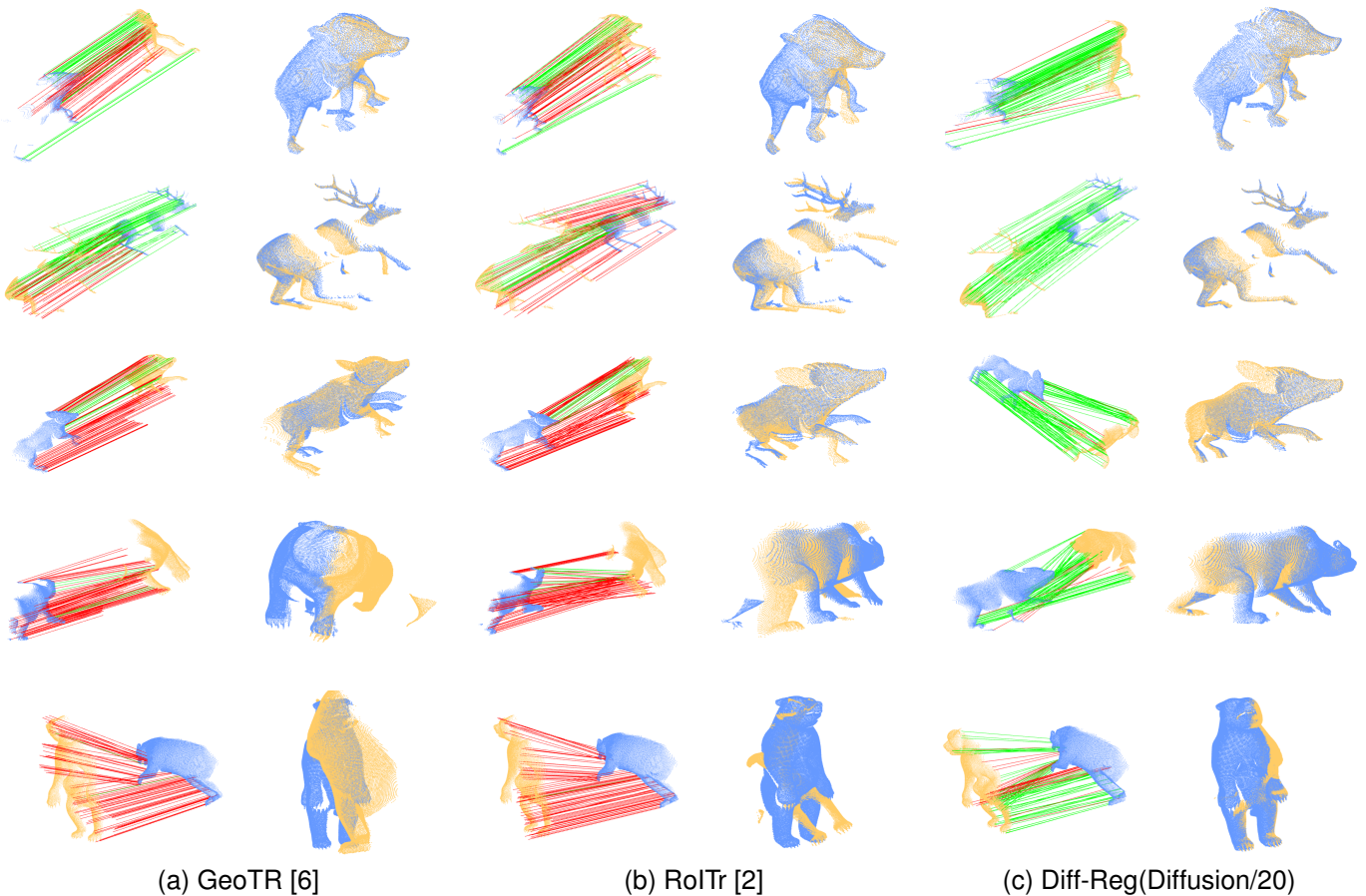


Fig. 4. The qualitative results of non-rigid registration in the 4DMatch/4DLoMatch benchmark. The top two lines are from 4DMatch, while the bottom three are from 4DLoMatch. The blue and yellow colors denote the source and target point cloud, respectively. The green and red lines indicate whether the threshold accepts the predicted deformable flow from the source points. The deformable registration is built by GraphSCNet [4]. Zoom in for details.

TABLE IV  
EVALUATION RESULTS ON RGB-D SCENES V2 [4]. THE BEST RESULTS ARE HIGHLIGHTED IN BOLD, AND THE SECOND-BEST RESULTS ARE UNDERLINED.

Model	Scene-11	Scene-12	Scene-13	Scene-14	Mean
Mean depth (m)	1.74	1.66	1.18	1.39	1.49
Inlier Ratio $\uparrow$					
FCGF-2D3D [65]	6.8	8.5	11.8	5.4	8.1
P2-Net [65]	9.7	12.8	17.0	9.3	12.2
Predator-2D3D [11]	17.7	19.4	17.2	8.4	15.7
2D3D-MATR [4]	32.8	34.4	<u>39.2</u>	23.3	32.4
FreeReg [38]	36.6	34.5	<u>34.2</u>	18.2	30.9
Diff-Reg(dino)	38.6	37.4	<b>45.4</b>	<u>31.6</u>	<u>38.3</u>
Diff-Reg(dino/backbone)	44.9	<b>49.5</b>	38.3	<b>33.1</b>	<b>41.4</b>
Diff-Reg(dino/diffusion/1)	<b>47.5</b>	<u>48.9</u>	32.8	22.4	37.9
Diff-Reg(dino/diffusion/10)	<u>47.2</u>	48.7	32.9	22.4	37.8
Feature Matching Recall $\uparrow$					
FCGF-2D3D [65]	11.10	30.40	51.50	15.50	27.10
P2-Net [65]	48.60	65.70	82.50	41.6	59.60
Predator-2D3D [11]	86.10	89.20	63.90	24.30	65.90
2D3D-MATR [4]	<u>98.60</u>	<u>98.00</u>	88.70	77.90	90.80
FreeReg [38]	91.90	93.40	<b>93.10</b>	49.60	82.00
Diff-Reg(dino)	<b>100.</b>	<b>100.</b>	89.70	<u>81.9</u>	<u>92.9</u>
Diff-Reg(dino/backbone)	<b>100.</b>	<b>100.</b>	92.8	<b>91.2</b>	<b>96.0</b>
Diff-Reg(dino/diffusion/1)	<b>100.</b>	<b>100.</b>	88.7	76.5	91.3
Diff-Reg(dino/diffusion/10)	<b>100.</b>	<b>100.</b>	88.7	77.0	91.4
Registration Recall $\uparrow$					
FCGF-2D3D [65]	26.4	41.2	37.1	16.8	30.4
P2-Net [65]	40.3	40.2	41.2	31.9	38.4
Predator-2D3D [11]	44.4	41.2	21.6	13.7	30.2
2D3D-MATR [4]	63.9	53.9	58.8	49.1	56.4
FreeReg+Kabsch [38]	38.7	51.6	30.7	15.5	34.1
FreeReg+PnP [38]	74.2	72.5	54.5	27.9	57.3
Diff-Reg(dino)	87.5	86.3	63.9	60.6	74.6
Diff-Reg(dino/backbone)	79.2	86.3	75.3	<b>71.2</b>	78.0
Diff-Reg(dino/diffusion/1)	<b>98.6</b>	<b>100.</b>	87.6	66.8	<b>88.3</b>
Diff-Reg(dino/diffusion/10)	<b>98.6</b>	<u>96.1</u>	83.5	63.7	85.5
Diff-Reg(dino/backbone <sub>epnp</sub> )	<u>95.8</u>	<u>96.1</u>	<b>88.7</b>	<u>69.0</u>	<u>87.4</u>

### B. 2D3D Registration Task: RGB-D SCENES V2

2D3D registration task is non-trivial because the 2D image data is a perspective projection of the 3D scene, which creates the scale ambiguity problem [4]. Since there is no good robust differentiable PnP [67] solver that can be integrated into our denoising module, we deploy the SOTA depth estimation model *Depth anything* [52] to generate “affine-invariant depth” for the image. Subsequently, we utilize the camera’s intrinsic matrix to project a point cloud onto a new non-metric point cloud, which is paired with the corresponding real point cloud in the dataset, creating a challenge scale ambiguous registration problem. To alleviate the scale ambiguity in the image data, we utilize the SOTA self-supervised foundation model *DINOv2* [39] to enhance the image features.

**Implementation Details.** For the single-pass backbone design, we follow 2D3D-MATR [4]. Specifically, for images in data pair, we utilize a ResNet [15] with FPN [68] to generate down-sampled superpixel and associated features. For the point cloud in the data pair, we exploit KPConv [14] to extract the down-sampled superpoint and associated features. A transformer [54] is deployed with inputs of superpixel and associated image features (including ResNet features and DINO features) from the image and superpoint and associated features from the target point cloud to predict the cross-modality features. The denoising transformer in  $g_\theta$  design has a similar definition. The new non-metric point cloud generated from the image depth

map of the Depth anything model [52] are used as inputs of the weighted SVD part in  $g_\theta$  to compute  $R, t$ . We utilize the coarse level circle loss [4] and fine level matching loss [4] for the single-pass backbone [4] and a focal loss for our denoising module  $g_\theta$ . The framework is trained and evaluated with PyTorch on one NVIDIA RTX 3090 GPU. We train our model about 30 epochs with batch size 1.

The overview of our framework for the 2D3D registration task is illustrated in Fig.5. We use Diff-Reg(dino) to denote the single-pass prediction head trained solely. Diff-Reg(dino/backbone) refers to the single-pass prediction head jointly trained with our denoising module  $g_\theta$ . Diff-Reg(dino/diffusion/#) denotes that the "Patch Matching" module in the top half (in Fig.5) is replaced with our denoising module (with # steps of reverse sampling). The coarse level image features  $F^{\hat{X}}$ ,  $F^{\hat{X}}_{dino}$ , and point features  $F^{\hat{Q}}$  are treated as const inputs of denoising module  $g_\theta$  in each reverse sampling step. For all variants of Diff-Reg(\*), we exclude the three scales "6 × 8, 12 × 16, 24 × 32" (refer to section 4.1 in [4]) after the coarsest level of ResNet and retain only "24 × 32". The visual features from DINOv2 [39] are combined with the coarsest level features that are upsampled to the finest level in ResNet. The training and reverse sampling process are listed in Algorithm.4 and Algorithm.5.

**Denoising Module  $g_\theta$  for 2D3D Registration.** In this section, we elucidate the functionality of our denoising module (see Fig.5). By leveraging the recent SOTA depth estimation model DepthAnything [52], we consider this non-metric depth as a constant input for each image. Diff-Reg(dino/backbone<sub>epnp</sub>) (in Table.IV) utilizes the EPnP solver [55] to compute the transformation  $R, t$ . Its high recall provides evidence that the implicit data augmentation from our diffusion model in matrix space indeed enhances the image backbone and the point cloud backbone. However, the EPnP solver's vulnerability to outliers during inference hinders its direct application in the reverse sampling process. Integrating the more robust PnP solver [69] into our denoising module could potentially remove the need for the depth estimation model. This improvement is an aspect we aim to explore in future research.

During inference, each reverse sampling step takes  $E^{t-1}$  from the previous step to provide initial correspondences. We then use either weighted SVD or the EPnP solver to calculate the transformation  $T^{t-1}$  that maps the point cloud  $\hat{Q}$  into the image plane space. Subsequently, we apply  $T^{t-1}$  to  $\hat{Q}$  to get warped  $\hat{Q}^{T^{t-1}}$ . Next, we use  $\hat{Q}^{T^{t-1}}$ ,  $\hat{X}$ ,  $F^{\hat{X}}_{dino}$ ,  $F^{\hat{X}}$ , and  $F^{\hat{Q}}$  as inputs of the transformer in  $g_\theta$  to compute the updated image features and point features for calculating the pseudo ground truth  $\hat{E}^0$ .

**Datasets.** RGB-D Scenes V2 [70] is generated from 14 indoor scenes with 11427 RGB-D frames. Following [4], we split 14 sequences of image-to-point-clouds pairs data, where scenes 0 – 8/9 – 10/11 – 14 for training/validation/testing. The resulting dataset contains 1748/236/497 image-to-point-cloud pairs.

**Metrics.** In this section, following [4], we give a detailed definition of three evaluation protocols: (1) Inlier Ratio (IR), the ratio of pixel-point matches whose 3D distance is under

---

**Algorithm 4** Training Diff-Reg in 2D-3D Registration Task

---

**Require:** Coarse level image and points  $\hat{X} \in \mathbb{R}^{\hat{H} \times \hat{W} \times 3}$ ,  $\hat{Q} \in \mathbb{R}^3$  and associated features  $F^{\hat{X}}$ ,  $F^{\hat{X}}_{dino}$ ,  $F^{\hat{Q}}$ .

- 1: **while** not converged **do**
- 2:   Sample  $E^0 \sim q(E^0)$
- 3:    $N \times M \leftarrow E^0.shape$
- 4:   Sample  $t \sim \text{Uniform}(1, \dots, T)$
- 5:    $\epsilon \sim \mathcal{N}(0, 1)^{N \times M}$
- 6:    $E^t \leftarrow \sqrt{\alpha_t} E^0 + \sqrt{1 - \alpha_t} f_\epsilon(\epsilon)$ ,  $\tilde{E}^t = E^t - \text{Min}(E^t)$
- 7:    $\hat{E}_0 \leftarrow g_\theta(\tilde{E}^t, \hat{X}, \hat{Q}, F^{\hat{X}}, F^{\hat{X}}_{dino}, F^{\hat{Q}})$
- 8:   Optimize  $L_t = \text{Focal\_loss}(\hat{E}_0, E^0)$
- 9: **end while**

---



---

**Algorithm 5** Sampling by Diff-Reg in 2D-3D Registration Task

---

**Require:** Initial matching matrix  $E^T$  from backbone or white noise; Coarse level image and points  $\hat{X} \in \mathbb{R}^{\hat{H} \times \hat{W} \times 3}$ ,  $\hat{Q} \in \mathbb{R}^3$  and associated features  $F^{\hat{X}}$ ,  $F^{\hat{X}}_{dino}$ ,  $F^{\hat{Q}}$ .

**Ensure:** Target matching matrix  $\tilde{E}^0$ .

- 1:  $N \times M \leftarrow E^T.shape$
- 2: **for**  $t = T, \dots, 1$  **do**
- 3:    $z_t \sim \mathcal{N}(0, 1)^{N \times M}$  if  $t > 1$  else  $z_t \leftarrow \mathbf{0}^{N \times M}$
- 4:    $\hat{E}_0 \leftarrow g_\theta(\tilde{E}^t, \hat{X}, \hat{Q}, F^{\hat{X}}, F^{\hat{X}}_{dino}, F^{\hat{Q}})$
- 5:    $\epsilon_t \leftarrow \frac{\hat{E}_0}{\sqrt{1 - \alpha_t}} - \frac{\sqrt{\alpha_t}}{\sqrt{1 - \alpha_t}} \tilde{E}^t$
- 6:    $\sigma_t \leftarrow \sqrt{\frac{(1 - \alpha_{t-1})}{1 - \alpha_t}} \sqrt{1 - \frac{\alpha_t}{\alpha_{t-1}}}$
- 7:    $\tilde{E}^{t-1} \leftarrow \sqrt{\alpha_{t-1}} \hat{E}_0 + \sqrt{1 - \alpha_{t-1} - \sigma_t^2} \epsilon_t + \sigma_t z_t$
- 8: **end for**
- 9:  $\tilde{E}^0 = \mathbf{f}_{\text{sinkhorn}}(\tilde{E}^0)$

---

a certain threshold (i.e., 5cm). (2) Feature Matching Recall (FMR), the ratio of image-to-point-cloud pairs whose inlier ratio is above a certain threshold (i.e., 10%). (3) Registration Recall (RR), the ratio of image-to-point-cloud pairs whose RMSE is under a certain threshold (i.e., 10cm).

**Quantitative results.** Following [4], we compare our diffusion matching model with FCGF [65], P2-Net [37], Predator [11], 2D3D-MATR [4], and FreeReg [38]. We introduce a robust single-pass baseline "Diff-Reg(dino)", in which we integrate the visual feature backbone DINOv2 [39] into the single-pass model 2D3D-MATR [4]. "Diff-Reg(dino/backbone)" represents the single-pass prediction head derived from "Diff-Reg(dino)" after joint training with our denoising module  $g_\theta$ . "Diff-Reg(Diffusion/1)" and "Diff-Reg(Diffusion/10)" refer to our diffusion matching model with one step and ten steps of reverse denoising sampling.

As demonstrated in Table IV, the results for "Diff-Reg(dino/backbone)" indicate that the diffused training samples in the matrix space serve as data augmentation to enhance the representation of the ResNet feature backbone and single-pass prediction head. Additionally, the outcome for "Diff-Reg(dino/diffusion/10)" illustrates that our denoising module  $g_\theta$  effectively tackles the scale ambiguous issue in 2D3D registration. Furthermore, the result for "Diff-Reg(dino/diffusion/1)" reveals that the diffused training samples within the matrix space indeed enhance the single-pass

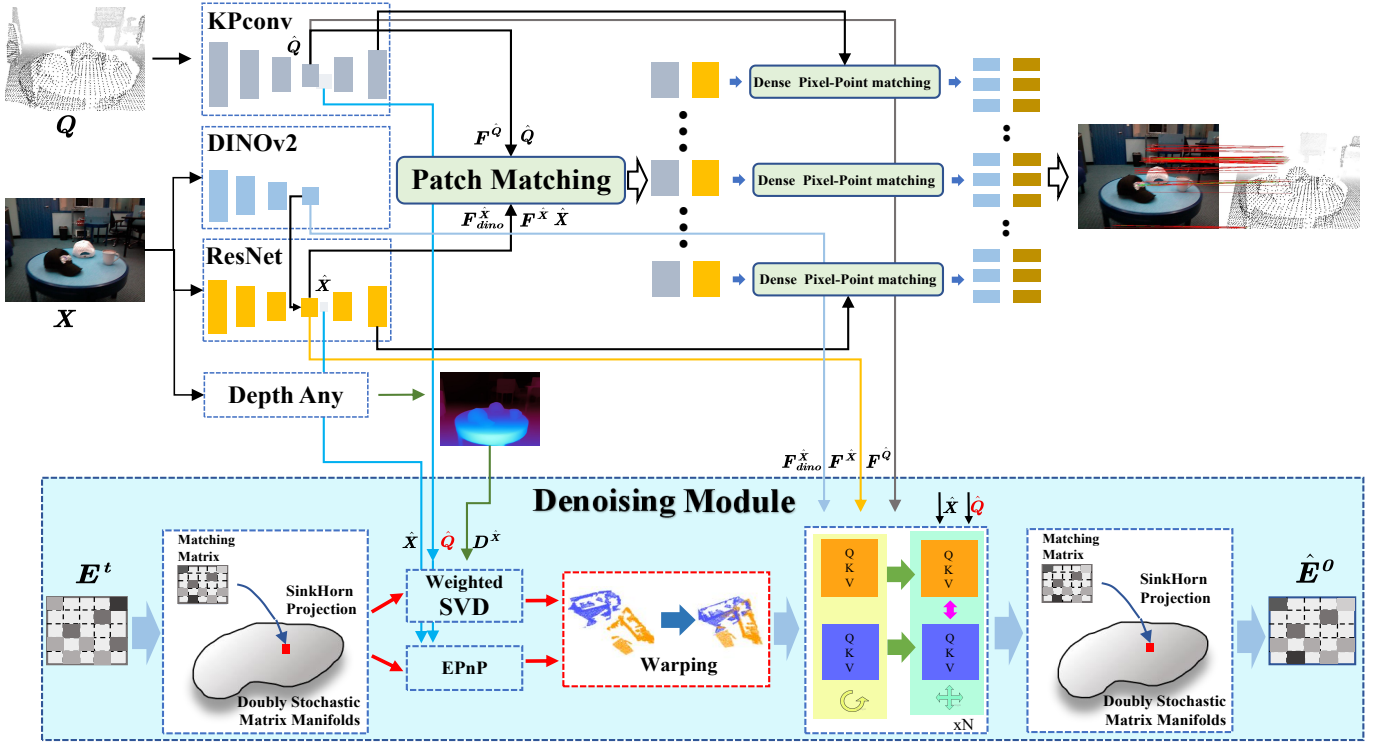


Fig. 5. Overview of our diffusion matching model framework for 2D/3D registration task: The top half (the gray part framed by the dashed line) is the **single-pass prediction head** with the backbones, while the bottom is our denoising module. The transformer in our denoising module utilizes the  $F^{\hat{X}}$ ,  $F^{\tilde{X}}$ ,  $F^{\hat{Q}}$ ,  $F^{\tilde{Q}}$ , and  $D^{\hat{X}}$  as inputs, while “patch matching” module in the single-pass head takes  $F^{\tilde{X}}$ ,  $F^{\tilde{Q}}$ ,  $F^{\hat{X}}$ , and  $\hat{Q}$  as inputs. Please zoom in for details.

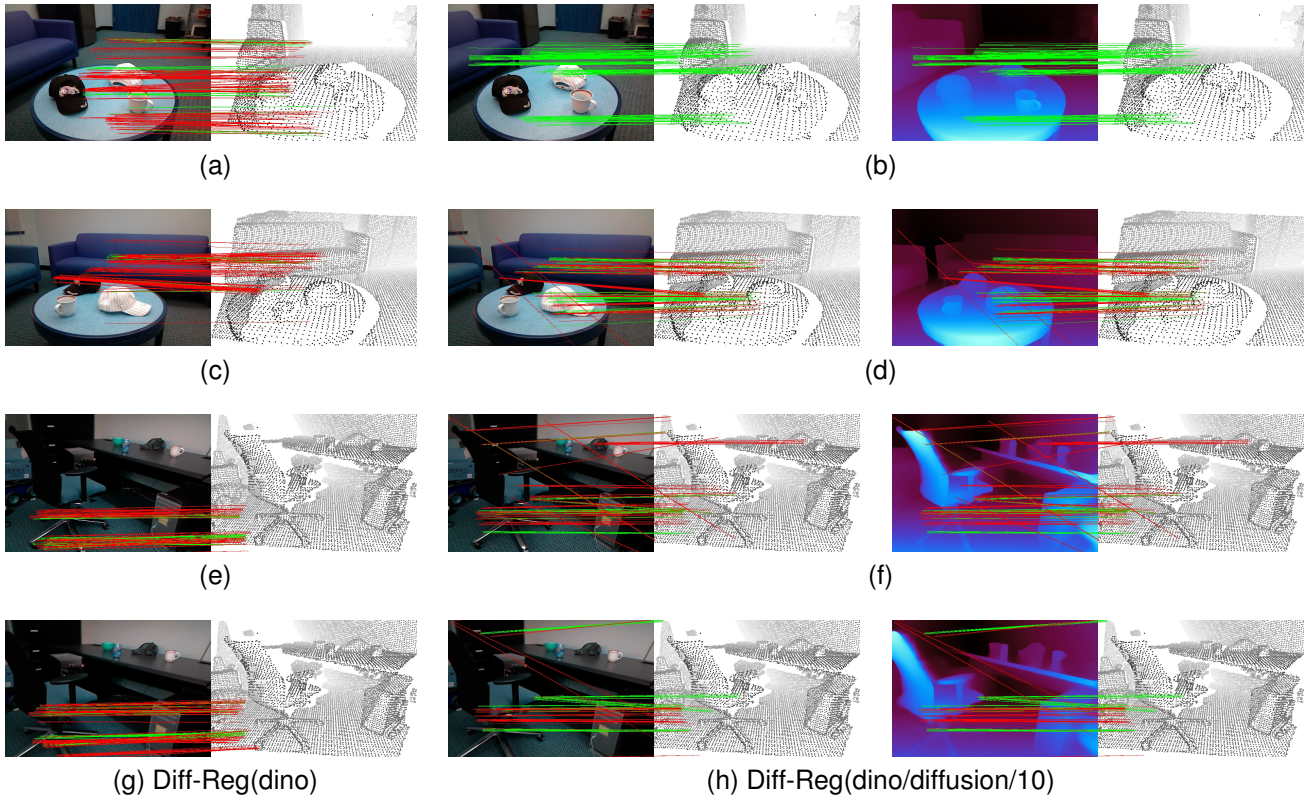


Fig. 6. The qualitative results of top-200 predicted correspondences on the RGB-D Scenes V2 benchmark [70]. The **green/red** color indicates whether the matching score is accepted based on a threshold value. Zoom in for details.

prediction head in “Diff-Reg(dino)”.

We also carried out an additional experiment to show that the performance improvement of “Diff-Reg(dino/backbone)” compared to “Diff-Reg(dino)” is attributed to our diffusion matching model. In this experiment, we did not use the depth map and instead employed one differentiable EPnP [67] solver in the denoising module  $g_\theta$  to replace the weighted SVD layer. We inputted only superpixels and superpoints with weights computed by associated superpixel and superpoint features. The single-pass prediction head “Diff-Reg(dino/backbone<sub>epnp</sub>)” (in Table IV) achieved a high recall rate of 87.4%, indicating that our diffused samples in matching matrix space indeed enhance the feature backbone.

**Qualitative results.** The examples of “Diff-Reg(dino/diffusion/10)” in Fig. 6 reveal that our diffusion matching model excels at capturing salient correspondences crucial for combinatorial consistency, regardless of their distance from the camera. On the other hand, the matches generated by “Diff-Reg(dino)” tend to be more focused at specific distances (from camera). For instance, in the third row, the correspondences produced by “Diff-Reg(dino)” are located very close to the camera, while the correspondences from “Diff-Reg(dino/diffusion/10)” encompass objects such as hats on the black table that are situated at a greater distance. In the first row, “Diff-Reg(dino)” fails to capture the correspondences on the sofa, and in the second row, the correspondences of the white hat on the table are lost. An extreme case in the fourth row demonstrates that “Diff-Reg(dino)” misses the farthest correspondence on the column bookshelf or wall. We provide more visualizations in Fig. 8 to illustrate our method’s effectiveness.

### C. Ablay Study and Discussion

**Capability of Escaping from Local Minima.** The DDPM framework is specifically designed for removing noise from perturbed samples. Typically, we begin with a baseline method that provides an initial solution, which can then be further refined to achieve better performance. To demonstrate that our denoising network has indeed learned the posterior distribution for the denoising module, we conducted an ablative experiment. In this experiment, we initiated reverse sampling from the solution obtained by the single-pass prediction head or from Gaussian white noise. In Table VI, the results of  $E_{Backbone}^T$  demonstrate that our denoising network can overcome local minima produced by the single-pass prediction head.

**Reverse Sampling Steps.** In our approach, we consider the denoising module as an optimizer that searches for the optimal matching matrix. We argue that increasing the number of search iterations may lead to better solutions. To validate this hypothesis, we experimented to investigate the impact of iterative searching steps on the results. We ran the reverse sampling step from 1 to 20 iterations. As shown in Table. VIII, the registration recall of our diffusion matching model increases as the number of sampling steps grows. The results prove that reverse sampling can reach a better solution by increasing the number of search steps.

**The lightweight design of our denoising module.** Due to the lightweight design, our denoising network showcases a notable speed enhancement compared to other concurrent diffusion-based methods for rigid point cloud registration. This efficiency improvement allows our approach to complete more denoising iterations. We have included a detailed list displaying the time costs (refer to Table VII) associated with each reverse denoising step, along with comparisons to recent studies. Our method achieves competitive results on the 3DMatch benchmark while maintaining fast processing speeds.

## V. CHALLENGES AND LIMITATIONS

As illustrated in Fig. 9, deformable registration encounters various challenges, including large motion, low overlap, sparse overlapping regions, and local non-rigid motion (e.g., the dress worn by the dancer in the last line of Fig. 9). Although our diffusion matching model is intended to address both rigid and deformable registration tasks, it may have inherent limitations. The transformer in our denoising module, along with the associated KPConv and ResNet backbone, follows a relatively generic design. To overcome these challenges, we acknowledge the importance of integrating more robust feature embedding techniques [2], [6] into our feature backbone for enhancements. Furthermore, incorporating task-specific priors into our denoising module could prove beneficial in addressing specific issues such as local non-rigid motion. We would leave these for future work.

The success of rigid registration with low overlapping relies on discriminative local feature embedding. The suboptimal performance of our method on the 3DLoMatch benchmark can be linked to the lack of integrated geometric embeddings, such as those mentioned in [2], [5], [6], [34], within feature backbone or transformer in our denoising module. We aim to address this as an area for improvement in future research.

## VI. CONCLUSION

This paper presents a novel diffusion module that leverages a diffusion matching model in the doubly stochastic matrix space to learn a posterior distribution for guiding the reverse denoising sampling process within the matrix space. Moreover, we have integrated a lightweight design into the denoising module to decrease the time cost associated with iterative reverse sampling. Experimental results on both 3D registration and 2D3D registration tasks confirm the effectiveness and efficiency of our proposed denoising module.

## REFERENCES

- [1] Y. Zhong, “Intrinsic shape signatures: A shape descriptor for 3d object recognition,” in *2009 IEEE 12th international conference on computer vision workshops, ICCV workshops*, 2009.
- [2] H. Yu, Z. Qin, J. Hou, M. Saleh, D. Li, B. Busam, and S. Ilic, “Rotation-invariant transformer for point cloud matching,” in *CVPR*, 2023.
- [3] X. Bai, Z. Luo, L. Zhou, H. Fu, L. Quan, and C.-L. Tai, “D3feat: Joint learning of dense detection and description of 3d local features,” in *CVPR*, 2020.
- [4] M. Li, Z. Qin, Z. Gao, R. Yi, C. Zhu, Y. Guo, and K. Xu, “2d3d-matr: 2d-3d matching transformer for detection-free registration between images and point clouds,” in *Proceedings of the IEEE/CVF International Conference on Computer Vision*, 2023.

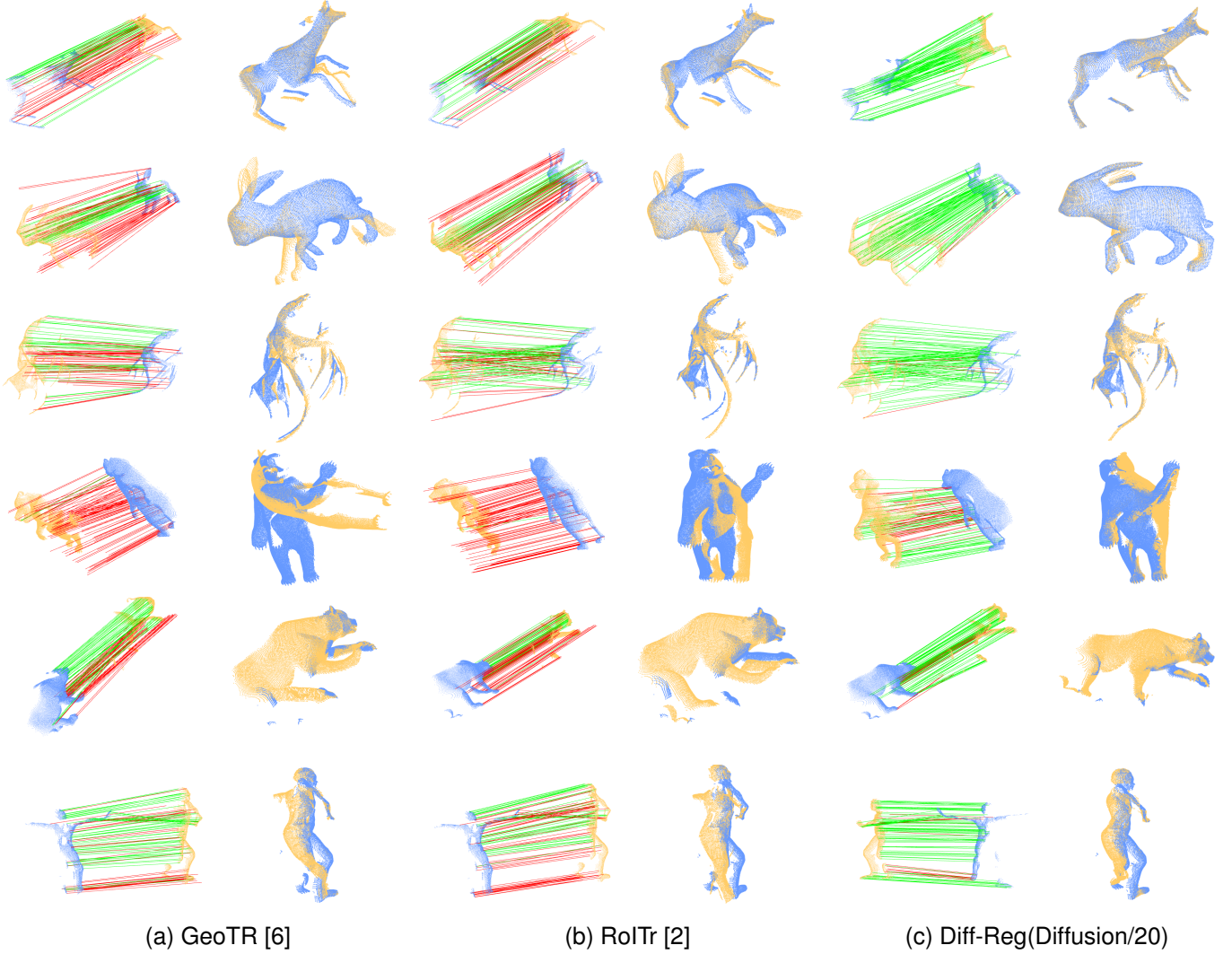


Fig. 7. More qualitative results of non-rigid registration in the 4DMatch/4DLoMatch benchmark. The blue and yellow colors denote the source and target point cloud, respectively. The green and red lines indicate whether the threshold accepts the predicted deformable flow from the source points. The deformable registration is built by GraphSCNet [59]. Zoom in for details.

TABLE VI

$E_{Backbone}^T$  DENOTE THE STARTING POINT WHERE  $E^T$  IS GENERATED BY THE SINGLE-PASS PREDICTION HEAD.  $E_{Gaussian}^T$  DENOTE THE STARTING POINT WHERE  $E^T$  IS SAMPLING FROM THE GAUSSIAN WHITE NOISE  $N(0, 1)^{N \times M}$ .  $z_t = 0$  DENOTES DETERMINISTIC SAMPLING, WHILE  $z_t \neq 0$  DENOTES THE RANDOM SAMPLING.

	$z_t \neq 0$						$z_t = 0$					
	3DMatch			3DLoMatch			3DMatch			3DLoMatch		
	FMR	IR	RR	FMR	IR	RR	FMR	IR	RR	FMR	IR	RR
$E_{Backbone}^T$	96.12	31.07	94.8	69.79	9.71	73.8	96.30	30.92	94.9	69.71	9.51	73.4
$E_{Gaussian}^T$	96.14	31.07	94.6	69.73	9.72	73.8	96.28	30.93	94.8	69.62	9.56	73.3
	$z_t \neq 0$				$z_t = 0$							
	4DMatch		4DLoMatch		4DMatch		4DLoMatch					
	NFMR	IR	NFMR	IR	NFMR	IR	NFMR	IR				
$E_{Backbone}^T$	88.38	86.38	75.94	67.64	88.34	86.36	76.22	67.82				
$E_{Gaussian}^T$	88.40	86.40	76.09	67.73	88.72	86.72	76.48	68.16				

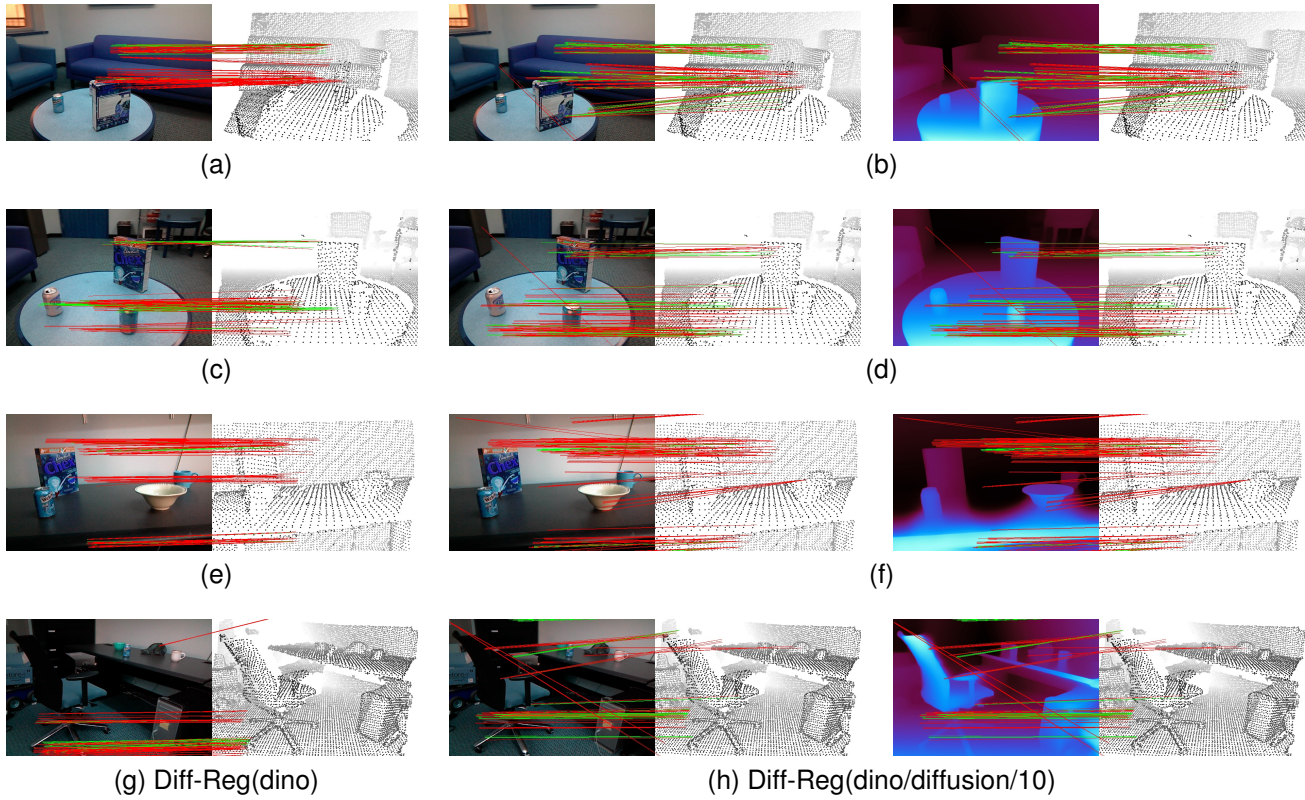


Fig. 8. More qualitative results on the RGB-D Scenes V2 benchmark [70]. The green/red color indicates whether the matching score is accepted based on a threshold value. Zoom in for details.

TABLE VII

COMPARISON OF TIME COST IN THE REVERSE SAMPLING STEP. THE BEST RESULTS ARE HIGHLIGHTED IN BOLD.

Iters	3DMatch		3DLoMatch	
	RR	Time(sec.)	RR	Time(sec.)
GeoTR [6]	92.0	0.296	74.0	0.284
GeoTR. + PEAL [33] 1-step	93.7	0.663	77.8	0.642
KPConv. + Diff-Reg 1-step	<b>94.8</b>	<b>0.048</b>	73.2	<b>0.052</b>
GeoTR. + PEAL [33] 5-step	94.0	2.131	78.5	2.074
KPConv. + Diff-Reg 5-step	<b>94.8</b>	<b>0.182</b>	73.7	<b>0.194</b>

TABLE VIII

THE ABLAY STUDY OF THE ITERATIVE STEPS OF REVERSE SAMPLING.

Iters	RR		NFMR/IR	
	3DMatch	3DLoMatch	4DMatch	4DLoMatch
1	94.8	73.3	85.34/83.93	73.11/65.26
10	94.8	73.4	87.99/86.07	75.46/67.15
20	95.0	73.8	88.39/86.64	76.16/67.82

[5] H. Deng, T. Birdal, and S. Ilic, "Ppfnet: Global context aware local features for robust 3d point matching," in *Proceedings of the IEEE conference on computer vision and pattern recognition*, 2018.

[6] Z. Qin, H. Yu, C. Wang, Y. Guo, Y. Peng, and K. Xu, "Geometric transformer for fast and robust point cloud registration," in *Proceedings of the IEEE/CVF Conference on Computer Vision and Pattern Recognition*, 2022.

[7] Q. Wu, Y. Ding, L. Luo, C. Zhou, J. Xie, and J. Yang, "Sgfeat: Salient geometric feature for point cloud registration," *arXiv preprint*

*arXiv:2309.06207*, 2023.

[8] Y. Li and T. Harada, "Lepard: Learning partial point cloud matching in rigid and deformable scenes," in *Proceedings of the IEEE/CVF Conference on Computer Vision and Pattern Recognition*, 2022.

[9] Z. J. Yew and G. H. Lee, "Regtr: End-to-end point cloud correspondences with transformers," in *Proceedings of the IEEE/CVF Conference on Computer Vision and Pattern Recognition*, 2022, pp. 6677–6686.

[10] G. Mei, H. Tang, X. Huang, W. Wang, J. Liu, J. Zhang, L. Van Gool, and Q. Wu, "Unsupervised deep probabilistic approach for partial point cloud registration," in *Proceedings of the IEEE/CVF Conference on Computer Vision and Pattern Recognition*, 2023.

[11] S. Huang, Z. Gojcic, M. Usvyatsov, A. Wieser, and K. Schindler, "Predator: Registration of 3d point clouds with low overlap," in *Proceedings of the IEEE/CVF Conference on computer vision and pattern recognition*, 2021.

[12] H. Yu, F. Li, M. Saleh, B. Busam, and S. Ilic, "Cofinet: Reliable coarse-to-fine correspondences for robust pointcloud registration," *Advances in Neural Information Processing Systems*, 2021.

[13] R. Yao, S. Du, W. Cui, A. Ye, F. Wen, H. Zhang, Z. Tian, and Y. Gao, "Hunter: Exploring high-order consistency for point cloud registration with severe outliers," *IEEE Transactions on Pattern Analysis and Machine Intelligence*, 2023.

[14] H. Thomas, C. R. Qi, J.-E. Deschaud, B. Marcotegui, F. Goulette, and L. J. Guibas, "Kpconv: Flexible and deformable convolution for point clouds," in *Proceedings of the IEEE/CVF international conference on computer vision*, 2019.

[15] K. He, X. Zhang, S. Ren, and J. Sun, "Deep residual learning for image recognition," in *Proceedings of the IEEE conference on computer vision and pattern recognition*, 2016.

[16] H. Yang, J. Shi, and L. Carlone, "Teaser: Fast and certifiable point cloud registration," *IEEE Transactions on Robotics*, vol. 37, no. 2, pp. 314–333, 2020.

[17] X. Bai, Z. Luo, L. Zhou, H. Chen, L. Li, Z. Hu, H. Fu, and C.-L. Tai, "Pointdsc: Robust point cloud registration using deep spatial consistency," in *Proceedings of the IEEE/CVF Conference on Computer Vision and Pattern Recognition*, 2021.

[18] Z. Chen, K. Sun, F. Yang, and W. Tao, "Sc2-pcr: A second order

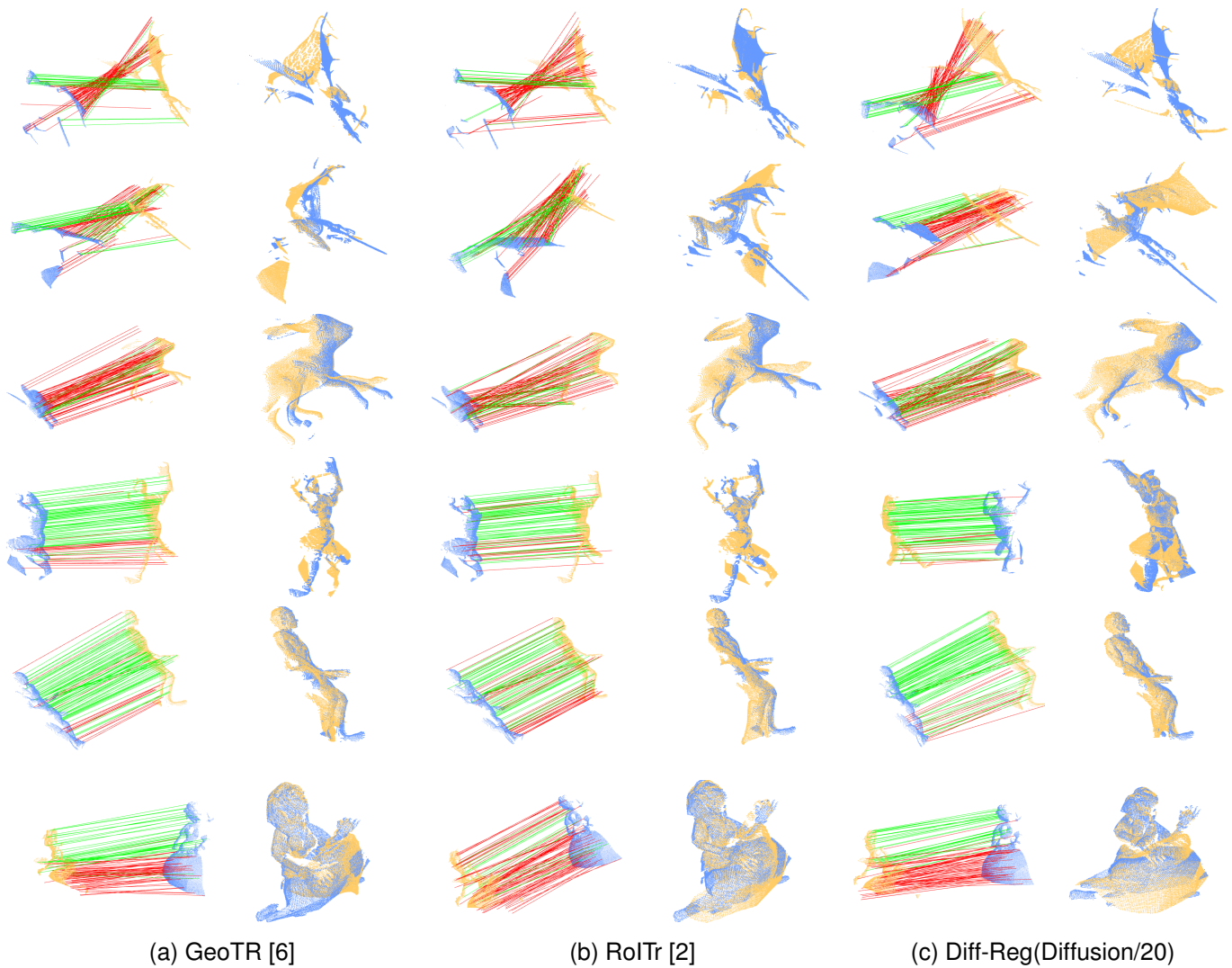


Fig. 9. Failure cases of our diffusion matching model on 4DMatch/4DLoMatch benchmark. The blue and yellow colors denote the source and target point cloud, respectively. The green and red lines indicate whether the threshold accepts the predicted deformable flow from the source points. The deformable registration is built by GraphSCNet [59]. Zoom in for details.

spatial compatibility for efficient and robust point cloud registration,” in *Proceedings of the IEEE/CVF Conference on Computer Vision and Pattern Recognition*, 2022.

[19] H. Jiang, Z. Dang, Z. Wei, J. Xie, J. Yang, and M. Salzmann, “Robust outlier rejection for 3d registration with variational bayes,” in *Proceedings of the IEEE/CVF Conference on Computer Vision and Pattern Recognition*, 2023.

[20] X. Zhang, J. Yang, S. Zhang, and Y. Zhang, “3d registration with maximal cliques,” in *Proceedings of the IEEE/CVF Conference on Computer Vision and Pattern Recognition*, 2023.

[21] C. R. Qi, O. Litany, K. He, and L. J. Guibas, “Deep hough voting for 3d object detection in point clouds,” in *proceedings of the IEEE/CVF International Conference on Computer Vision*, 2019.

[22] K. Fu, S. Liu, X. Luo, and M. Wang, “Robust point cloud registration framework based on deep graph matching,” in *CVPR*, 2021.

[23] J. Ho, A. Jain, and P. Abbeel, “Denosing diffusion probabilistic models,” *Advances in neural information processing systems*, 2020.

[24] J. Song, C. Meng, and S. Ermon, “Denosing diffusion implicit models,” *arXiv preprint arXiv:2010.02502*, 2020.

[25] C. Vignac, I. Krawczuk, A. Siraudin, B. Wang, V. Cevher, and P. Frossard, “Digress: Discrete denosing diffusion for graph generation,” *arXiv preprint arXiv:2209.14734*, 2022.

[26] J. Austin, D. D. Johnson, J. Ho, D. Tarlow, and R. Van Den Berg, “Structured denosing diffusion models in discrete state-spaces,” *Advances in Neural Information Processing Systems*, vol. 34, pp. 17981–17993, 2021.

[27] R. M. Caron, X. Li, P. Mikusiński, H. Sherwood, and M. D. Taylor, “Nonsquare “doubly stochastic” matrices,” *Lecture Notes-Monograph Series*, vol. 28, pp. 65–75, 1996. [Online]. Available: <http://www.jstor.org/stable/4355884>

[28] Q. Wu, Y. Shen, H. Jiang, G. Mei, Y. Ding, L. Luo, J. Xie, and J. Yang, “Graph matching optimization network for point cloud registration,” in *2023 IEEE/RSJ International Conference on Intelligent Robots and Systems (IROS)*, 2023.

[29] G. Mei, X. Huang, L. Yu, J. Zhang, and M. Bennamoun, “Cotreg: Coupled optimal transport based point cloud registration,” *arXiv preprint arXiv:2112.14381*, 2021.

[30] Y. Li and T. Harada, “Non-rigid point cloud registration with neural deformation pyramid,” *Advances in Neural Information Processing Systems*, 2022.

[31] A. Zeng, S. Song, M. Nießner, M. Fisher, J. Xiao, and T. Funkhouser, “3dmatch: Learning local geometric descriptors from rgb-d reconstructions,” in *Proceedings of the IEEE conference on computer vision and pattern recognition*, 2017, pp. 1802–1811.

[32] H. Yu, J. Hou, Z. Qin, M. Saleh, I. Shugurov, K. Wang, B. Busam, and S. Ilic, “Riga: Rotation-invariant and globally-aware descriptors for point cloud registration,” *arXiv preprint arXiv:2209.13252*, 2022.

[33] J. Yu, L. Ren, Y. Zhang, W. Zhou, L. Lin, and G. Dai, “Peal: Prior-embedded explicit attention learning for low-overlap point cloud registration,” in *CVPR*, 2023.

[34] H. Deng, T. Birdal, and S. Ilic, “Ppf-foldnet: Unsupervised learning of rotation invariant 3d local descriptors,” in *Proceedings of the European*

- Conference on Computer Vision (ECCV)*, 2018.
- [35] Z. Chen, Y. Ren, T. Zhang, Z. Dang, W. Tao, S. Süssstrunk, and M. Salzmann, "Diffusionpcr: Diffusion models for robust multi-step point cloud registration," *arXiv preprint arXiv:2312.03053*, 2023.
- [36] J. Li and G. H. Lee, "Deepi2p: Image-to-point cloud registration via deep classification," *2021 IEEE/CVF Conference on Computer Vision and Pattern Recognition (CVPR)*, 2021.
- [37] B. Wang, C. Chen, Z. Cui, J. Qin, C. X. Lu, Z. Yu, P. Zhao, Z. Dong, F. Zhu, N. Trigoni, and A. Markham, "P2-net: Joint description and detection of local features for pixel and point matching," *2021 IEEE/CVF International Conference on Computer Vision (ICCV)*, 2021.
- [38] H. Wang, Y. Liu, B. Wang, Y. Sun, Z. Dong, W. Wang, and B. Yang, "Freereg: Image-to-point cloud registration leveraging pretrained diffusion models and monocular depth estimators," *ArXiv*, 2023.
- [39] M. Oquab, T. Darcet, T. Moutakanni, H. Vo, M. Szafraniec, V. Khalidov, P. Fernandez, D. Haziza, F. Massa, A. El-Nouby *et al.*, "Dinov2: Learning robust visual features without supervision," *arXiv preprint arXiv:2304.07193*, 2023.
- [40] Y. Song and S. Ermon, "Generative modeling by estimating gradients of the data distribution," *Advances in neural information processing systems*, 2019.
- [41] J. Gong, L. G. Foo, Z. Fan, Q. Ke, H. Rahmani, and J. Liu, "Diffpose: Toward more reliable 3d pose estimation," *2023 IEEE/CVF Conference on Computer Vision and Pattern Recognition (CVPR)*, 2022.
- [42] W. Shan, Z. Liu, X. Zhang, Z. Wang, K. Han, S. Wang, S. Ma, and W. Gao, "Diffusion-based 3d human pose estimation with multi-hypothesis aggregation," *2023 IEEE/CVF International Conference on Computer Vision (ICCV)*, 2023.
- [43] J. Wang, C. Rupprecht, and D. Novotný, "Posediffusion: Solving pose estimation via diffusion-aided bundle adjustment," *2023 IEEE/CVF International Conference on Computer Vision (ICCV)*, 2023.
- [44] S. Chen, P. Sun, Y. Song, and P. Luo, "Diffusiondet: Diffusion model for object detection," in *Proceedings of the IEEE/CVF International Conference on Computer Vision*, 2023.
- [45] D. Baranchuk, I. Rubachev, A. Voynov, V. Khrlukov, and A. Babenko, "Label-efficient semantic segmentation with diffusion models," *ArXiv*, 2021.
- [46] Z. Gu, H. Chen, Z. Xu, J. Lan, C. Meng, and W. Wang, "Diffusioninst: Diffusion model for instance segmentation," *ArXiv*, 2022.
- [47] G. Parisi, "Correlation functions and computer simulations," *Nuclear Physics B*, 1981.
- [48] J. Urain, N. Funk, J. Peters, and G. Chalvatzaki, "Se (3)-diffusionfields: Learning smooth cost functions for joint grasp and motion optimization through diffusion," in *2023 IEEE International Conference on Robotics and Automation (ICRA)*, 2023.
- [49] H. Jiang, M. Salzmann, Z. Dang, J. Xie, and J. Yang, "Se (3) diffusion model-based point cloud registration for robust 6d object pose estimation," *arXiv preprint arXiv:2310.17359*, 2023.
- [50] M. Cuturi, "Sinkhorn distances: Lightspeed computation of optimal transport," *Advances in neural information processing systems*, 2013.
- [51] T.-Y. Lin, P. Dollár, R. B. Girshick, K. He, B. Hariharan, and S. J. Belongie, "Feature pyramid networks for object detection," *IEEE Conference on Computer Vision and Pattern Recognition (CVPR)*, 2016.
- [52] L. Yang, B. Kang, Z. Huang, X. Xu, J. Feng, and H. Zhao, "Depth anything: Unleashing the power of large-scale unlabeled data," *arXiv preprint arXiv:2401.10891*, 2024.
- [53] P. J. Besl and N. D. McKay, "Method for registration of 3-d shapes," in *Sensor fusion IV: control paradigms and data structures*, 1992.
- [54] A. Vaswani, N. Shazeer, N. Parmar, J. Uszkoreit, L. Jones, A. N. Gomez, Ł. Kaiser, and I. Polosukhin, "Attention is all you need," *Advances in neural information processing systems*, 2017.
- [55] S. Li, C. Xu, and M. Xie, "A robust o (n) solution to the perspective-n-point problem," *IEEE transactions on pattern analysis and machine intelligence*, 2012.
- [56] K. S. Arun, T. S. Huang, and S. D. Blostein, "Least-squares fitting of two 3-d point sets," *IEEE Transactions on pattern analysis and machine intelligence*, 1987.
- [57] R. W. Sumner, J. Schmid, and M. Pauly, "Embedded deformation for shape manipulation," in *ACM siggraph 2007*, 2007.
- [58] T. Igarashi, T. Moscovich, and J. F. Hughes, "As-rigid-as-possible shape manipulation," *ACM transactions on Graphics (TOG)*, 2005.
- [59] Z. Qin, H. Yu, C. Wang, Y. Peng, and K. Xu, "Deep graph-based spatial consistency for robust non-rigid point cloud registration," in *Proceedings of the IEEE/CVF Conference on Computer Vision and Pattern Recognition*, 2023.
- [60] B. Mildenhall, P. P. Srinivasan, M. Tancik, J. T. Barron, R. Ramamoorthi, and R. Ng, "Nerf: Representing scenes as neural radiance fields for view synthesis," *Communications of the ACM*, 2021.
- [61] Y. Li, H. Takehara, T. Taketomi, B. Zheng, and M. Nießner, "4dcomplete: Non-rigid motion estimation beyond the observable surface," in *ICCV*, 2021.
- [62] W. Wu, Z. Wang, Z. Li, W. Liu, and L. Fuxin, "Pointpwc-net: A coarse-to-fine network for supervised and self-supervised scene flow estimation on 3d point clouds," *arXiv preprint arXiv:1911.12408*, 2019.
- [63] G. Puy, A. Boulch, and R. Marlet, "Flot: Scene flow on point clouds guided by optimal transport," in *European conference on computer vision*, 2020.
- [64] X. Li, J. Kaeseemodel Pontes, and S. Lucey, "Neural scene flow prior," *Advances in Neural Information Processing Systems*, 2021.
- [65] C. Choy, J. Park, and V. Koltun, "Fully convolutional geometric features," in *Proceedings of the IEEE/CVF International Conference on Computer Vision*, 2019.
- [66] J. Lee, M. Cho, and K. M. Lee, "Hyper-graph matching via reweighted random walks," in *CVPR*, 2011.
- [67] V. Lepetit, F. Moreno-Noguer, and P. Fua, "Ep n p: An accurate o (n) solution to the p n p problem," *International journal of computer vision*, 2009.
- [68] T.-Y. Lin, P. Dollár, R. Girshick, K. He, B. Hariharan, and S. Belongie, "Feature pyramid networks for object detection," in *Proceedings of the IEEE conference on computer vision and pattern recognition*, 2017.
- [69] H. Chen, P. Wang, F. Wang, W. Tian, L. Xiong, and H. Li, "Epro-ppn: Generalized end-to-end probabilistic perspective-n-points for monocular object pose estimation," in *Proceedings of the IEEE/CVF Conference on Computer Vision and Pattern Recognition*, 2022, pp. 2781–2790.
- [70] K. Lai, L. Bo, and D. Fox, "Unsupervised feature learning for 3d scene labeling," in *IEEE International Conference on Robotics and Automation (ICRA)*, 2014.